JEM Journal of Experimental Medicine

ARTICLE

IRF7 controls spontaneous autoimmune germinal center and plasma cell checkpoints

Adam J. Fike[1], Kristen N. Bricker[1,2], Michael V. Gonzalez[4], Anju Maharjan[2], Tien Bui[2], Keomonyroth Nuon[2], Scott M. Emrich[3], Julia L. Weber[1,2], Sara A. Luckenbill[1], Nicholas M. Choi[1], Renan Sauteraud[5], Dajiang J. Liu[5], Nancy J. Olsen[6], Roberto Caricchio[7], Mohamed Trebak[3], Sathi Babu Chodisetti[1,2], and Ziaur S.M. Rahman[1,2]

How IRF7 promotes autoimmune B cell responses and systemic autoimmunity is unclear. Analysis of spontaneous SLE-prone mice deficient in IRF7 uncovered the IRF7 role in regulating autoimmune germinal center (GC), plasma cell (PC), and autoantibody responses and disease. IRF7, however, was dispensable for foreign antigen–driven GC, PC, and antibody responses. Competitive bone marrow (BM) chimeras highlighted the importance of IRF7 in hematopoietic cells in spontaneous GC and PC differentiation. Single-cell RNAseq of SLE-prone B cells indicated IRF7-mediated B cell differentiation through GC and PC fates. Mechanistic studies revealed that IRF7 promoted B cell differentiation through GC and PC fates by regulating the transcriptome, translation, and metabolism of SLE-prone B cells. Mixed BM chimeras demonstrated a requirement for B cell–intrinsic IRF7 in IgG autoantibody production but not in the regulation of spontaneous GC and PC responses. Altogether, we delineate previously unknown B cell–intrinsic and –extrinsic mechanisms of IRF7-promoted spontaneous GC and PC responses, loss of tolerance, autoantibody production, and SLE development.

Introduction

Systemic lupus erythematosus (SLE) is a debilitating autoimmune disease initiated by dysregulated B cell responses and the emergence of autoreactive B cells (Karrar and Cunninghame Graham, 2018; Nashi et al., 2010; Rawlings et al., 2017). Autoreactive B cells in SLE produce antinuclear antibodies (ANA) that deposit as immune complexes (ICs) in various tissues, including kidneys and vasculature, causing inflammation and end-organ disease (Bagavant and Fu, 2009). Genetic predisposition in concert with TLR activation by self-nucleic acid, permits B cell escape of tolerance mechanisms, leading to the emergence of autoreactive B cells (Celhar and Fairhurst, 2014; Christensen and Shlomchik, 2007; Green et al., 2009). TLR signaling promotes aberrant differentiation of autoreactive B cells into plasma cell (PC) and germinal center (GC) cells to generate autoantibody-producing B cells (Brown et al., 2022; Christensen et al., 2006; Deane et al., 2007; Jackson et al., 2014; Soni et al., 2014); however, the signals downstream of TLR activation and the mechanisms that regulate autoreactive B cells in SLE remain unclear.

We and others previously demonstrated a B cell–intrinsic requirement for TLR7 in promoting autoimmune GC and PC responses and systemic autoimmunity (Brown et al., 2022; Christensen et al., 2006; Cosgrove et al., 2023; Deane et al., 2007; Hwang et al., 2012; Jackson et al., 2014; Soni et al., 2014). Stimulation of endosomal TLRs by nucleic acids, including TLR7, activates NFκB family members and IFN regulatory factors 5 (IRF5) and 7 (IRF7). To date, numerous studies have characterized the involvement of IRF5 and IRF5 risk variants in SLE in mice and humans (Ban et al., 2021; Banga et al., 2020; Cham et al., 2012; Pellerin et al., 2021; Richez et al., 2010). IRF7 was previously shown to promote autoantibody responses but not lupus nephritis in a chemically (pristane)-induced B6 model of SLE (Miyagawa et al., 2016). IRF7 risk alleles are also implicated in the development of human SLE (Salloum et al., 2010; Yasuda et al., 2007). However, IRF7-expressing cell type(s) and mechanisms by which IRF7 drives autoreactive B cell differentiation through PC and GC checkpoints, leading to autoantibody-secreting PCs and autoantibody production in SLE, remain

[1]Department of Microbiology and Immunology, Pennsylvania State University College of Medicine, Hershey, PA, USA; [2]Department of Microbiology and Immunology, Thomas Jefferson University, Philadelphia, PA, USA; [3]Department of Cellular and Molecular Physiology, Pennsylvania State University College of Medicine, Hershey, PA, USA; [4]Center for Cytokine Storm Treatment and Laboratory, Perelman School of Medicine, University of Pennsylvania, Philadelphia, PA, USA; [5]Public Health Science, Pennsylvania State University College of Medicine, Hershey, PA, USA; [6]Rheumatology, Pennsylvania State University College of Medicine, Hershey, PA, USA; [7]Rheumatology, UMass Chan Medical School, Worcester, MA, USA.

Correspondence to Ziaur S.M. Rahman: ziaur.rahman2@jefferson.edu

M. Trebak's current affiliation is Pharmacology and Chemical Biology, University of Pittsburgh, Pittsburgh, PA, USA.
A preprint of this paper was posted in *bioRxiv* on February 8, 2025.

unknown. IRF7 has long been thought to contribute to SLE by regulating type 1 IFN (T1-IFN) production by plasmacytoid dendritic cells (pDCs) (Honda et al., 2005; Yasuda et al., 2007), although IRF7 is also expressed in B cells and monocytes (Ning et al., 2011). Whether and how IRF7 may promote autoimmune GC and PC responses, autoantibody production, and disease in spontaneous SLE models via functioning in cell types other than pDCs is unknown. It is also unclear whether IRF7 transcriptionally controls SLE-promoting gene programs in B cells other than T1-IFN genes.

Here, using FcγRIIB$^{-/-}$ and FcγRIIB$^{-/-}$Yaa spontaneous SLE mouse models, we identified a major role for IRF7 in promoting spontaneous autoimmune PC, GC, and autoantibody responses and SLE-like disease but not in foreign antigen–driven PC, GC, and antibody responses. Single-cell RNA sequencing (scRNAseq) of B cells from FcγRIIB$^{-/-}$ IRF7$^{-/-}$ and FcγRIIB$^{-/-}$ control mice indicated a role for IRF7-driven genetic programs in regulating B cell differentiation through pre-GC to GC and PC populations. Mixed bone marrow (BM) competition chimeras demonstrated a role for IRF7 expression in hematopoietic compartments in driving GC and PC but not myeloid or T cell responses in FcγRIIB$^{-/-}$ mice. Using B cell–specific mixed BM chimeras, we further demonstrated a B cell–intrinsic requirement of IRF7 in the production of class-switched IgG autoantibodies but not for promoting overall spontaneous autoimmune PC and GC responses. Together, we delineate B cell–intrinsic and –extrinsic functions for IRF7 in regulating B cell transcription, translation, and metabolism, and in breaching tolerance and promoting autoimmune GC and PC responses and systemic autoimmunity development.

Results

IRF7 promotes autoimmune GC and PC responses in spontaneous SLE models

To identify the mechanisms by which IRF7 regulates autoimmune GC and PC responses and systemic autoimmunity, we crossed IRF7-deficient (IRF7$^{-/-}$) mice with well-characterized SLE-prone FcγRIIB$^{-/-}$ mice (Bolland et al., 2002; Richez et al., 2010; Shinde et al., 2018). FcγRIIB$^{-/-}$ mice were originally generated on a 129 background and backcrossed to B6 mice for several generations (Bolland et al., 2002; Richez et al., 2010; Shinde et al., 2018). We further backcrossed FcγRIIB$^{-/-}$ mice to B6 for at least N12–14 generations prior to intercrossing and then crossing with IRF7-deficient mice. FcγRIIB$^{-/-}$ mice in our colony are deficient in the *Fcgr2b* gene and carry 129-derived signaling lymphocyte activation molecule (*Slam*) family genes that are tightly linked to the *Fcgr2b* gene (Soni et al., 2015). FcγRIIB$^{-/-}$ mice had many of the manifestations of human SLE, including splenomegaly with the increased number of splenocytes (Fig. S1, A–C), elevated GC and PC responses, ANAs, and renal disease (Fig. 1 and Fig. S1, A–C) (Bolland et al., 2002; Shinde et al., 2018; Soni et al., 2015). IRF7-deficient FcγRIIB$^{-/-}$ mice (FcγRIIB$^{-/-}$IRF7$^{-/-}$) had reduced spleen size and splenocyte number, reduced GC, effector T cell (Teff) and T follicular helper (Tfh) cell, and PC (Fig. 1, A–H and Fig. S1, A–C) responses at 2, 4, and 6 mo of ages. FcγRIIB$^{-/-}$IRF7$^{-/-}$ mice had reduced numbers of autoantibody-producing antibody-forming cells (AFCs) in the spleen and BM (Fig. 1, I and J) and dampened serum ANA reactivity (Fig. 1 K).

In FcγRIIB$^{-/-}$ mice, autoantibodies started accumulating at 2 mo of age, while at this time point only nucleosome-specific serum IgM, IgG, and IgG2c titers were reduced in IRF7-deficient mice (Fig. S1, D–F). Nucleosome-, double stranded deoxyribonucleic acid (dsDNA), and Smith Ribonucleoprotein (SmRNP)-specific IgG and IgG2c titers were significantly reduced in FcγRIIB$^{-/-}$IRF7$^{-/-}$ mice at 4 and 6 mo of age when substantial amounts of autoantibodies accumulated in FcγRIIB$^{-/-}$ mice (Fig. 1, L–N). We also found reduced numbers of IgG1- and IgG2c-producing, but not total IgG- and IgG3-producing, splenic and BM AFCs in FcγRIIB$^{-/-}$IRF7$^{-/-}$ mice compared with FcγRIIB$^{-/-}$ control mice (Fig. S2, A and B). In addition, total serum IgG, IgG1, IgG2c, and IgG3 titers were lower in FcγRIIB$^{-/-}$IRF7$^{-/-}$ mice than in FcγRIIB$^{-/-}$ control mice (Fig. S2 C). IC deposition and immune cell infiltration in the kidney (Fig. 1, O and P) and kidney pathology (Fig. 1 Q) and scoring for glomerulonephritis, interstitial nephritis, and vessels (Fig. 1 R) were significantly reduced in FcγRIIB$^{-/-}$IRF7$^{-/-}$ mice. FcγRIIB$^{-/-}$IRF7$^{-/-}$ mice also had reduced myeloid cell populations, including conventional DCs and monocyte-derived DCs, although the frequency and number of pDCs were increased (Fig. S3).

Splenomegaly (Fig. 2 A), GC and PC responses (Fig. 2, B–E), and age-associated B cell (ABC) responses, as well as Teff and Tfh cell responses (Fig. 2, G and H), were also reduced in IRF7-deficient FcγRIIB$^{-/-}$yaa male mice (Fig. 2 F) that express two copies of TLR7 and present with robust and rapid systemic autoimmune responses and disease (Bolland et al., 2002; Richez et al., 2010). Additionally, FcγRIIB$^{-/-}$yaaIRF7$^{-/-}$ mice showed reduced numbers of autoantibody-producing splenic and BM AFCs (Fig. S4, A and B) and reduced serum titers of IgG and IgG2c autoantibodies to RNA-associated antigen, SmRNP (Fig. 2 I). However, no significant changes were observed in myeloid cell responses except for a consistent increase in the number of pDCs in the absence of IRF7 (Fig. S4, C and D). High-dimensional flow cytometry analysis of immune cell populations within the kidneys of these mice showed significant reductions in the number of CD45$^+$ cells, inflammatory DCs (iDCs), macrophages, natural killer (NK) cells, and CD8$^+$ Teffs, but not B cells, pDCs, monocyte-derived DCs, conventional DCs, monocytes, neutrophils, and CD4$^+$ Teffs in the absence of IRF7 (Fig. 2, J and K). In addition, FcγRIIB$^{-/-}$yaaIRF7$^{-/-}$ mice had reduced serum blood urea nitrogen (BUN) and creatinine levels (Fig. 2, L and M), indicators of improved renal function. Finally, FcγRIIB$^{-/-}$yaaIRF7$^{-/-}$ mice had improved overall survival (Fig. 2 N).

Together, combined data from two SLE mouse models reinforce the role of IRF7 in controlling spontaneous autoimmune GC and PC responses, leading to autoantibody production and the development of SLE-like disease.

IRF7 is dispensable for foreign antigen–driven GC, PC, and antibody responses in both non-autoimmune and SLE-prone mice

We next determined the role of IRF7 in foreign antigen–driven GC, PC, and antibody responses by immunizing B6 control and

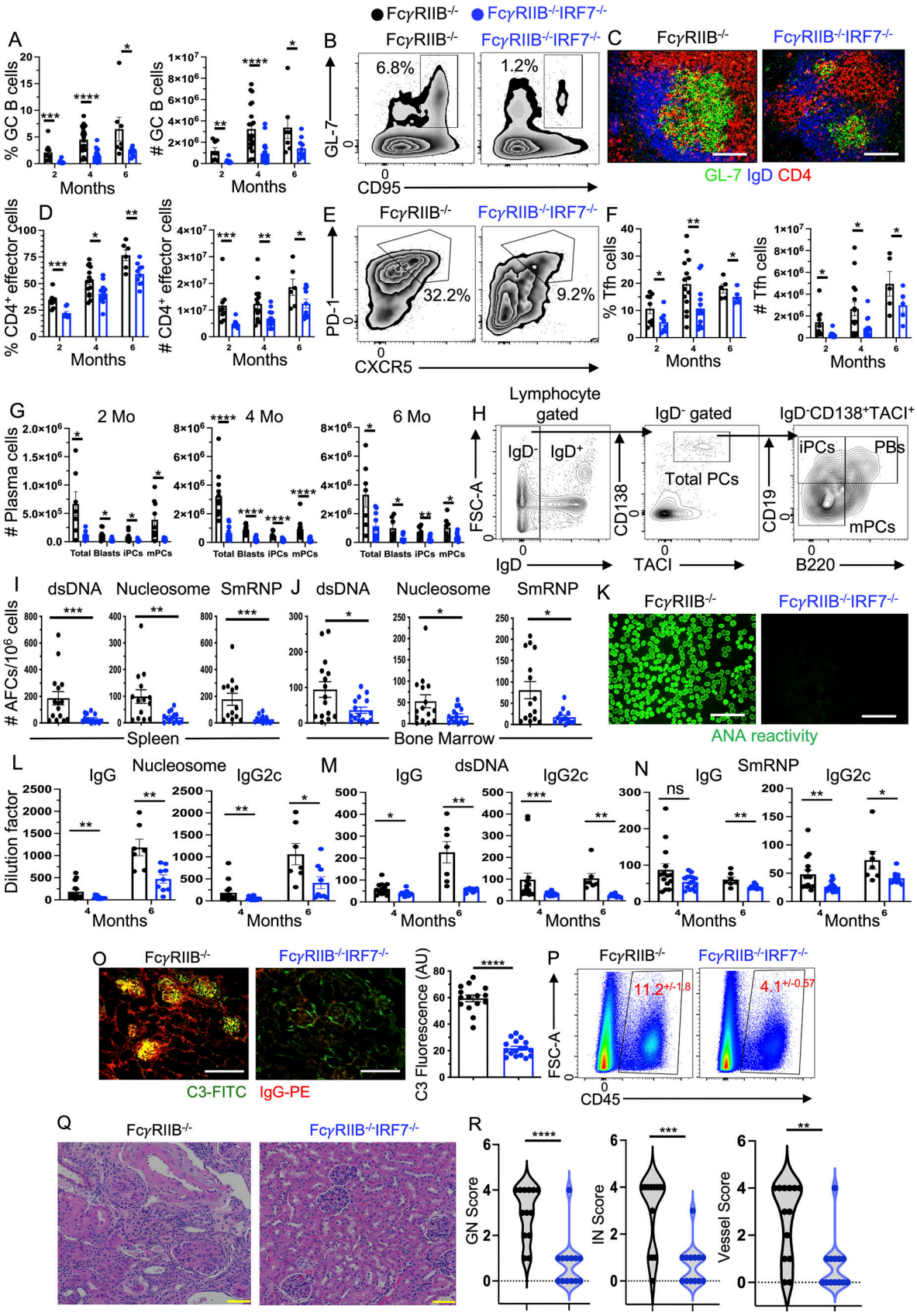

Figure 1. **IRF7 promotes autoimmunity in the FcγRIIB$^{-/-}$ mouse model of SLE. (A–H)** B and T cell responses were evaluated in the spleens of FcγRIIB$^{-/-}$ and FcγRIIB$^{-/-}$IRF7$^{-/-}$ mice at 2, 4, and 6 mo time points. **(A)** Frequency and number of B220^{+}GL-7^{+}CD95^{+} GC B cells of total B220^{+} B cells. **(B)** Representative flow plots showing the gating strategy of GC B cells. **(C)** Representative images showing IgD^{-}GL-7^{+} GC B cells and CD4^{+} Tfh cells within the GC by staining

splenic sections with anti-IgD (blue), GL-7 (green), and anti-CD4 (red). Scale bars, 100 µm. **(D)** Frequency and number of $CD4^+CD44^+CD62L^-$ Teffs of total $CD4^+$ cells. **(E and F)** (E) Flow cytometry gating strategy and (F) frequency and number of $CD4^+CD44^+CD62L^-CXCR5^+PD\text{-}1^+$ Tfh of total $CD4^+$ cells. **(G and H)** (G) Number and (H) flow cytometry gating strategy of $CD138^+TACI^+$ total PCs gated on IgD^- cells from lymphocyte gated populations, followed by gating on $CD138^+TACI^+$ total PCs for B220 and CD19 expression to identify $B220^+CD19^+$ plasmablast (PB), $B220^-CD19^+$ immature (iPC), and $B220^-CD19^-$ mature (mPC) PCs based on B220 and CD19 expression. **(I and J)** ELISpot assay quantifying the number of dsDNA-, nucleosome-, and SmRNP-specific (I) splenic and (J) BM AFCs from 4-mo-old mice. **(K)** Hep-2 immunofluorescent (IF) images showing ANA seropositivity in 4-mo-old mice. Scale bars, 100 µm. **(L–N)** (L) Nucleosome-, (M) dsDNA-, and (N) SmRNP-specific serum IgG and IgG2c titers. **(O)** IF images of kidney sections showing $C3^+$ (green) and IgG^+ (red) IC deposition. Scale bars, 100 µm. **(P)** Flow cytometry plots showing the gating strategy and frequency of $CD45^+$ immune cells in the kidney. **(Q and R)** (Q) Representative images of kidney sections from 6-mo-old mice were stained with periodic acid–Schiff and (R) the pathology score for glomerulonephritis (GN), interstitial nephritis (IN), and vessels. Scale bars, 50 µm. Each symbol (panels A–P and R) represents an individual mouse (n = 7–22 mice per group), and data are presented as means ± SEM. Data in panels A to R represent two to four experiments per time point. P values were calculated via two-way ANOVA with Sidak multiple comparisons test (A–G) or an unpaired Student's t test (I–R) (*, P < 0.05; **, P < 0.01; ***, P < 0.001; ****, P < 0.0001). ns, not significant.

$IRF7^{-/-}$ mice with 4-hydroxy-3-nitrophenylacetyl-KLH (NP-KLH) in CFA. We observed no differences in the frequencies of total and NP-specific B cell and GC B cell responses between the strains 14 days after NP-KLH immunization (Fig. 3, A–D). Total and NP-specific $CD138^+TACI^+$ PC responses were similar between the strains except for an increased frequency of immature PCs in IRF7-deficient mice (Fig. 3, E–H). $IRF7^{-/-}$ mice had a reduced percentage of Teffs, although no difference in Tfh frequency between the strains was observed (Fig. 3, I and J). We also observed no differences in high- (NP_4) and low- (NP_{28}) affinity NP-specific IgG and IgG1 Ab responses (Fig. 3, K and L). We then immunized autoimmune-prone mice sufficient and deficient in IRF7 during ongoing autoimmune responses. Consistent with the data observed in non-autoimmune B6 and $IRF7^{-/-}$ mice, we found no differences in the frequencies of total and NP-specific B cell and GC B cell responses between $FcγRIIB^{-/-}$ and $FcγRIIB^{-/-}IRF7^{-/-}$ mice 14 days after NP-KLH immunization (Fig. 4, A–D). $FcγRIIB^{-/-}IRF7^{-/-}$ mice had reduced total PCs but showed increased frequencies of plasmablasts, immature PCs, and NP^+ PCs (Fig. 4, E–H). $FcγRIIB^{-/-}IRF7^{-/-}$ mice further had no deficits in Teff and Tfh (Fig. 4, I and J) and low- and high-affinity NP-specific IgG and IgG1 antibody responses (Fig. 4, K and L). Together, findings from SLE-associated and immunization-induced responses in both non-autoimmune and autoimmune-prone mice highlight a critical role of IRF7 in promoting systemic autoimmune responses but not foreign antigen–induced GC, PC, and antibody responses.

IRF7 expression in the hematopoietic compartments drives spontaneous GC and PC responses in $FcγRIIB^{-/-}$ mice

To determine the effects of IRF7 expression in the host microenvironment versus the hematopoietic compartment on autoimmune GC and PC responses in $FcγRIIB^{-/-}$ mice, we generated competitive mixed BM chimeras. Lethally irradiated wild-type hosts ($CD45.1^+$) received a 50:50 mix of BM from $FcγRIIB^{-/-}$ ($CD45.1^+CD45.2^+$) and $FcγRIIB^{-/-}IRF7^{-/-}$ ($CD45.2^+$) donors (Fig. 5 A). 8 wk after reconstitution, recipient mice were equally reconstituted by both donor populations (Fig. 5 B). Analysis of B cell populations revealed no significant differences in the development of naïve follicular B cells (Fig. 5, C and D) or ABCs (Fig. 5, E and F). However, we observed a significant reduction in IRF7-deficient B cells within splenic GC (Fig. 5, G and H) and PC responses within the spleen and BM (Fig. 5, I and J). Interestingly, IRF7 deficiency in hematopoietic cells did not affect Teff and Tfh populations (Fig. 5, K and L), and numerous myeloid populations except for iDCs, which remained significantly reduced, and pDCs, which were elevated in the absence of IRF7 (Fig. 5 M). These findings suggest the importance of IRF7 expression in hematopoietic cells in B cell differentiation into GC B cells and PCs during systemic autoimmune responses in $FcγRIIB^{-/-}$ mice.

Single-cell transcriptome of SLE-prone B cells identifies 14 clusters and their regulation by IRF7-driven transcriptional programs

Given the effects of IRF7 expression in hematopoietic cells on spontaneous B cell responses, we next examined the role of IRF7 in transcriptional control of B cell responses in SLE by performing scRNAseq on splenic B cells sorted from 3-mo-old $FcγRIIB^{-/-}IRF7^{-/-}$ and $FcγRIIB^{-/-}$ mice. To be able to detect transcriptome in subsets of splenic-activated B cells that represent a small percentage of cells compared with naïve B cells, analysis was performed on B cells composed of 90% IgD^- antigen-experienced B cells and 10% IgD^+ naïve B cells (Fig. 6 A and Fig. S5 A). Unsupervised clustering of 36,842 B cells passing quality control identified 14 B cell clusters as visualized using Uniform Manifold Approximation and Projection (UMAP) (Fig. 6 B; and Fig. S5, B and C). These B cell clusters were annotated based on the expression of canonical markers specific for subpopulations of B cells (Fig. 6 C) and by comparing our new data set with the annotated scRNAseq previously reported by others (Laidlaw et al., 2020). We identified a sharp reduction in the percentage of $IRF7^{-/-}$ B cells in the pre-GC transition, GC dark and light zones, and PC/blast clusters, but not in the follicular cluster 2, marginal zone (MZ), or switched activated populations (Fig. 6, D and E). Transitional and follicular cluster 1 and naïve-activated B cells were proportionally higher in $IRF7^{-/-}$ B cells than control cells (Fig. 6 E). In summary, scRNAseq of autoimmune B cells sufficient and deficient in IRF7 identified 14 clusters and revealed significant differences in subpopulations of B cells, pointing to potential regulation of autoimmune GC and PC responses by IRF7-driven transcriptional programs.

IRF7-driven transcriptome in B cells regulates B cell differentiation through pre-GC, GC, and PC populations during a systemic autoimmune response

To determine the role of IRF7 in B cell differentiation into the GC and PC pathways, we analyzed the top 100 genes differentially

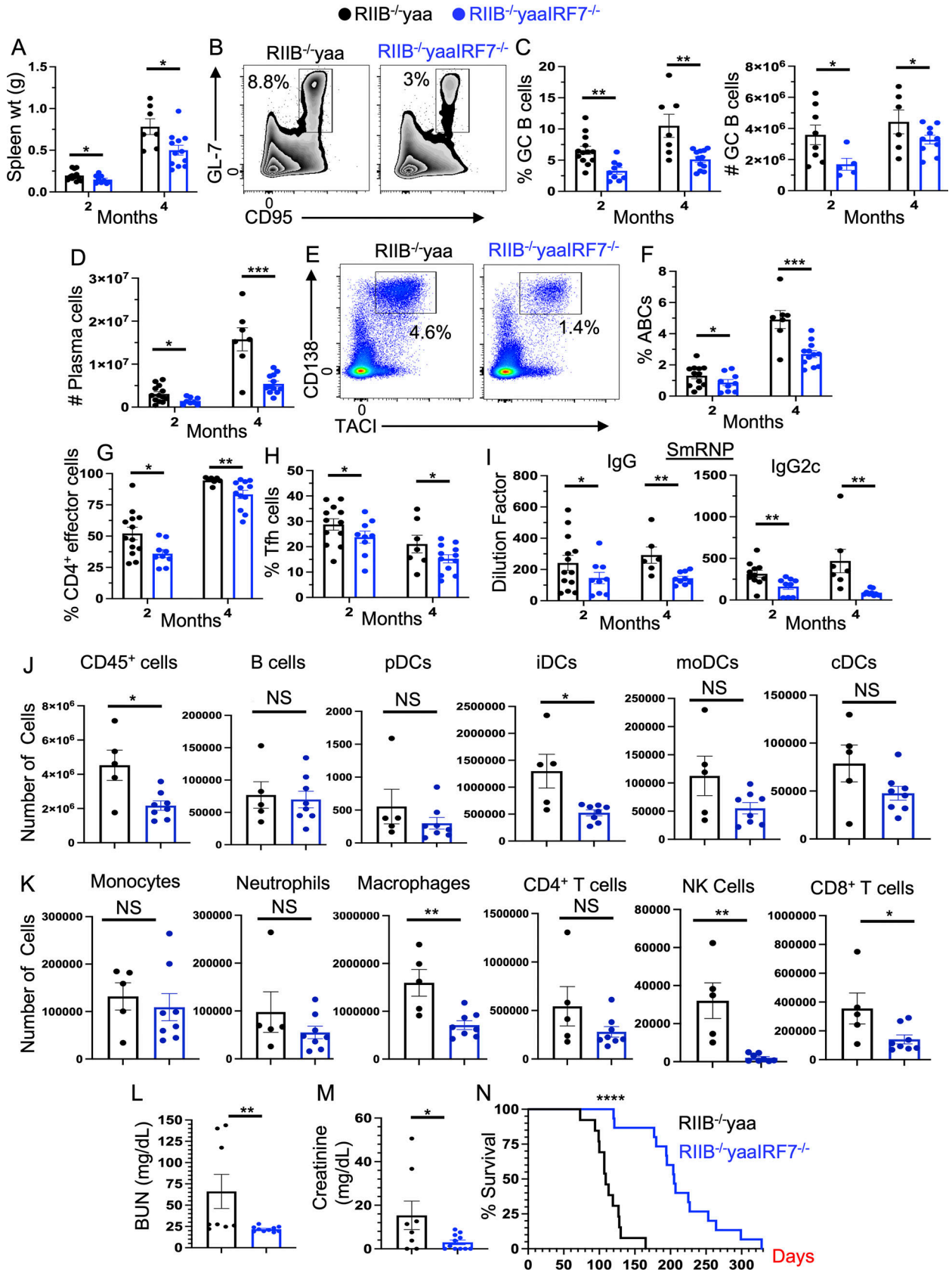

Figure 2. **The contribution of IRF7 to a TLR7-driven FcγRIIB$^{-/-}$ model of SLE. (A–H)** B and T cell responses were evaluated in the spleens of FcγRIIB$^{-/-}$yaa (RIIB$^{-/-}$yaa) and FcγRIIB$^{-/-}$yaaIRF7$^{-/-}$ (RIIB$^{-/-}$yaaIRF7$^{-/-}$) mice at 2 and 4 mo of age. **(A)** Spleen weight of RIIB$^{-/-}$yaa and RIIB$^{-/-}$yaaIRF7$^{-/-}$ mice. **(B and C)** (B) Flow cytometry gating strategy and (C) frequency and number of B220^{+}GL-7^{+}CD95^{+} GC B cells of total B220^{+} B cells. **(D and E)** (D) Number and (E) flow

cytometry gating strategy and frequency of CD138$^+$TACI$^+$ PCs in IgD$^-$ B cells. **(F)** Frequency of IgD$^-$CD11b$^+$CD11c$^+$ ABCs of B220$^+$CD19$^+$ B cells in the spleen. **(G and H)** Frequency of (G) CD4$^+$CD44$^+$CD62L$^-$ Teffs of total CD4$^+$ cells and (H) CD4$^+$CD44$^+$CD62L$^-$CXCR5$^+$PD-1$^+$ Tfh of total CD4$^+$ cells. **(I)** Serum IgG and IgG2c anti-SmRNP antibodies were measured by ELISA. **(J and K)** High-dimensional flow cytometry analysis of kidney immune cell infiltrates identifying following populations: total CD45$^+$ cells, CD45$^+$CD11b$^-$CD19$^+$B220$^+$ B cells, CD45$^+$CD19$^-$CD11b$^-$CD11c$^+$B220$^+$CD317$^+$ pDCs, CD45$^+$CD19$^-$B220$^-$CD56$^-$CD11b$^+$CD11c$^+$MHCII^{hi} iDCs, CD45$^+$CD19$^-$B220$^-$CD56$^-$CD11b$^+$CD11c$^+$Ly6c$^+$Ly6G$^-$ moDCs, CD45$^+$CD19$^-$B220$^-$CD56$^-$CD11b$^-$CD11c$^+$MHCII$^+$ cDCs, CD45$^+$CD19$^-$B220$^-$CD56$^-$CD11b$^+$Ly6C$^+$Ly6G$^-$ monocytes, CD45$^+$CD19$^-$B220$^-$CD56$^-$CD11b$^+$Ly6C$^+$Ly6G$^+$ neutrophils, CD345$^+$B220$^-$CD19$^-$CD56$^-$CD11b$^+$F4/80$^+$MHCII$^+$ macrophages, CD45$^+$CD19$^-$B220$^-$CD11b$^-$CD4$^+$CD44$^+$CD62L$^-$ CD4$^+$ Teffs, CD45$^+$CD11b$^-$B220$^-$CD19$^-$CD4$^-$CD8$^-$CD56$^+$ NK cells, and CD45$^+$CD19$^-$B220$^-$CD11b$^-$CD8$^+$CD44$^+$CD62L$^-$ CD8$^+$ Teffs. **(L and M)** (L) BUN and (M) creatinine levels were measured in sera collected from 4-mo-old mice. **(N)** The percentage of survival in RIIB$^{-/-}$yaa and RIIB$^{-/-}$yaaIRF7$^{-/-}$ mice. Each symbol represents an individual mouse, and data are presented as means ± SEM. Data in panels A–I and N (n = 7–13 mice per group) represent three experiments. Data in panels J–M (n = 5–11 mice per group) represent two to three experiments. P values were calculated via two-way ANOVA with Dunn–Sidak correction (A–K), an unpaired Student's t test (L), Mann–Whitney test (M), or log-rank (Mantel–Cox) test (N) (*, P < 0.05; **, P < 0.01; ***, P < 0.001; ****, P < 0.0001). NS, not significant; cDCs, conventional DCs; moDCs, monocyte-derived DCs.

expressed between IRF7-sufficient and -deficient B cells across the scRNAseq dataset and identified dynamic transcriptional changes associated with B cell differentiation (Fig. 7 A). To further investigate the involvement of IRF7 in regulating B cell differentiation, we used pseudotime inference to identify transcriptional programs associated with B cell differentiation (Fig. 7 B). The pseudotime trajectory revealed that B cells differentiated in two major pathways: one group differentiated through a pre-GC transitional bridge into GC and PC clusters, and the other group into naïve activated and switched activated B cells and MZ B cells (Fig. 7 B), which can contribute to the generation of autoantibody-producing cells and autoantibodies. We found that IRF7 deficiency in B cells predominantly affected B cell differentiation from pre-GC clusters into GC and PC clusters. We further re-clustered the pre-GC transitional B cell cluster from our scRNAseq dataset to identify underlying subpopulations and their regulation by IRF7 (Fig. 7 C). The re-clustered pre-GC transitional B cells produced five subclusters that allowed further examination. We examined these five subclusters for gene markers associated with B cell differentiation and manually annotated the five subclusters based on cluster-based gene expression. Pre-GC1 expressed numerous genes that distinguished them from naïve follicular B cells, but they retained the most follicular markers in the subcluster. As B cells differentiated through pre-GC stages, they downregulated follicular B cell markers (*Cd38*, *Klf2*, and *S1pr1*) and began to upregulate markers of activation/GC differentiation (Fig. 7 D, *S1pr2*, *Aicda*, *Mef2b*, *Mef2c*, *Pou2f2*, *Ezh2*, *Fas*, *J chain*, and *Slamf7*). Further analysis of scRNAseq data indicated that cells of the pre-GC1 cluster were quiescent, followed by proliferation of B cells at pre-GC2 and pre-GC3 clusters (Fig. 7, E and G). Finally, we determined the percentage of each subcluster that was composed of FcγRIIB$^{-/-}$ or FcγRIIB$^{-/-}$IRF7$^{-/-}$ B cells and found a stark reduction in FcγRIIB$^{-/-}$IRF7$^{-/-}$ B cells starting at the pre-GC2 cluster (Fig. 7, E and F). These data indicate that IRF7-driven genetic programs regulate B cell differentiation at the pre-GC stages during spontaneous autoimmune B cell responses in SLE-prone FcγRIIB$^{-/-}$ mice.

IRF7 promotes systemic autoimmunity by regulating transcription, translation, and metabolism in activated B cells

To understand the B cell–intrinsic mechanism of IRF7-mediated systemic autoimmunity, we performed pathway analysis on differentially expressed genes identified between FcγRIIB$^{-/-}$ and FcγRIIB$^{-/-}$IRF7$^{-/-}$ mice within the pre-GC clusters of the scRNAseq. The top two pathways identified contained translation (EIF2 signaling) and oxidative phosphorylation (OXPHOS)–related genes, including ribosomal genes that were differentially expressed between FcγRIIB$^{-/-}$ and FcγRIIB$^{-/-}$IRF7$^{-/-}$ pre-GC clusters (Fig. 8, A and B). We also performed IRF7 chromatin immunoprecipitation (ChIP)-seq on antigen-experienced IgD$^-$ B cells from FcγRIIB$^{-/-}$ mice and identified 1229 IRF7 peaks, and ∼32% mapped within 3 kb of a promoter, and the remainder fell largely within intergenic regions or introns (Fig. 8 C). Combined scRNAseq and ChIP-seq analysis identified overlap between 42 upregulated and 29 downregulated genes between FcγRIIB$^{-/-}$ and FcγRIIB$^{-/-}$ IRF7$^{-/-}$ B cells that were IRF7 targets (Fig. 8 D). Surprisingly, we found IRF7 peaks in the promoters of several ribosomal protein genes (Fig. 8 E). To validate the OXPHOS pathway identified in the scRNAseq data set (Fig. 8 A), we performed extracellular flux analysis, which revealed lower OXPHOS and glycolysis in FcγRIIB$^{-/-}$IRF7$^{-/-}$ B cells compared with FcγRIIB$^{-/-}$ control B cells, including basal respiration and non-mitochondrial O_2 consumption rate (OCR) (Fig. 8, F and G). The differences in the OXPHOS pathway were not a consequence of different proportions of B cell subsets between the two groups. Our analysis of peripheral B cell subsets showed no major differences (data not shown) in the proportions of B cell subsets in the spleens between the two groups except for GC B cells and PCs (Fig. 1). Thus, we do not believe that differences in GC and PC frequency and number, which represent about 5% of total B cells, can alone make up for substantial differences we observed in OCR and extracellular acidification rate (ECAR) values of total B cells between the two groups. To validate the EIF2 signaling pathway (Fig. 8 A) linked to translation, we measured translation and found that FcγRIIB$^{-/-}$IRF7$^{-/-}$ GC B cells and PCs had reduced translation compared with FcγRIIB$^{-/-}$ control B cell counterparts (Fig. 8 H). FcγRIIB$^{-/-}$IRF7$^{-/-}$ B cells also showed reduced translation compared with FcγRIIB$^{-/-}$ control B cells after TLR7 stimulation but not IgM and CD40 (Fig. 8 I). These data suggest that IRF7 transcriptionally regulates translation and metabolism in B cells, promoting SLE-associated GC and PC responses.

B cell–intrinsic IRF7 is required for loss of tolerance and autoantibody production but not sufficient for promoting overall spontaneous GC and PC responses

Given the effects of IRF7 on B cell transcriptome, translation, and metabolism, we measured IRF7 levels in B cell subsets in FcγRIIB$^{-/-}$ mice. IRF7 expression was elevated in pre-GC and GC B cells relative to non-GC B cells, with the highest expression in

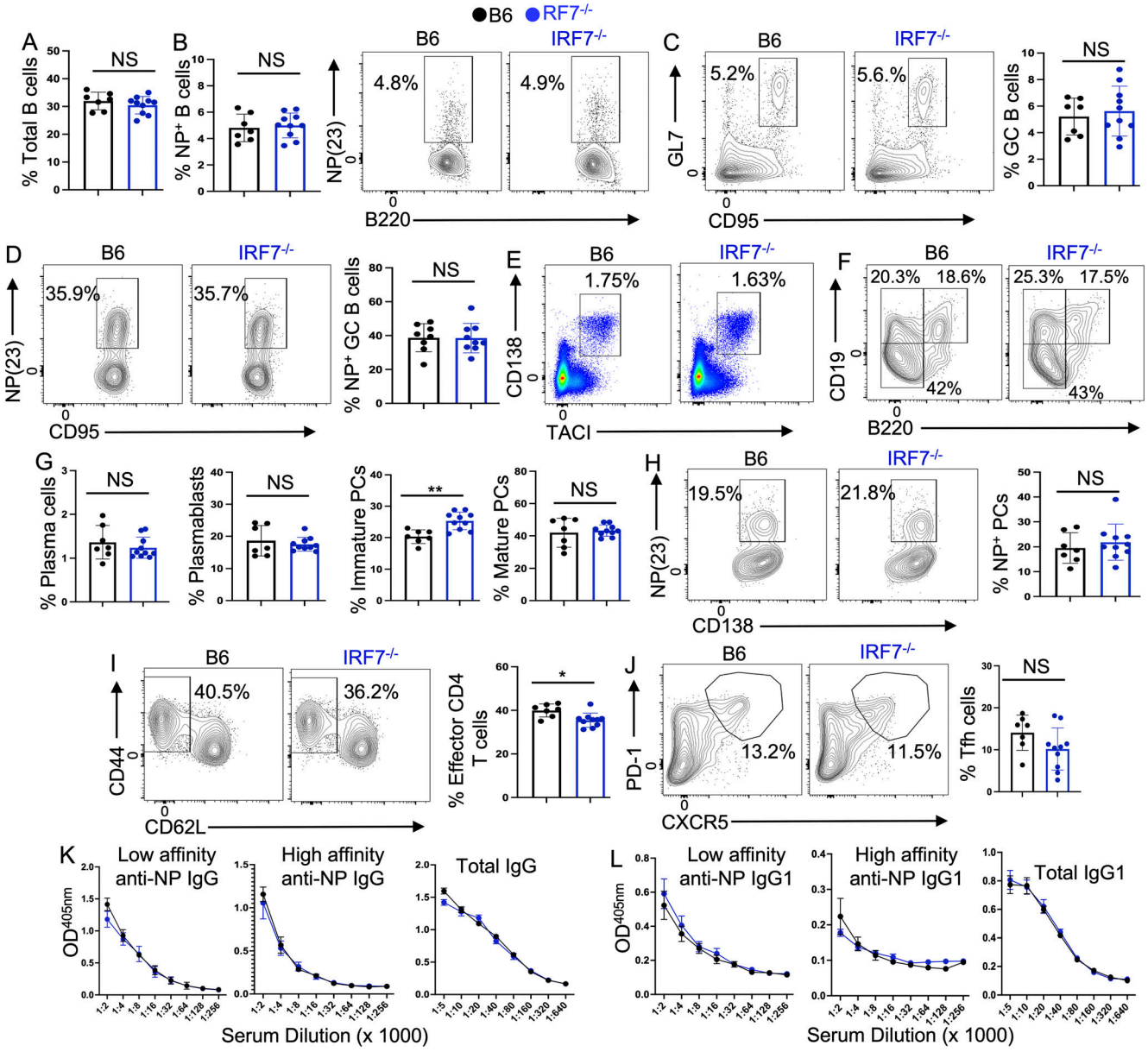

Figure 3. **IRF7 signaling is not required for foreign antigen–driven GC, PC, and Ab responses in non-autoimmune mice.** 8- to 10-wk-old age- and sex-matched IRF7-deficient ($IRF7^{-/-}$, blue circles) and C57BL/6 (B6, black circles) control mice were immunized with NP-KLH in CFA as described in Materials and methods. **(A and B)** The splenic GC, PC, and antibody responses were analyzed on 14 days after immunization. Frequencies of (A) $B220^+$ total and (B) $B220^+NP^+$ B cells. **(C)** Frequency of $B220^+GL\text{-}7^+CD95^+$ GC B cells of total $B220^+$ B cells. **(D)** Frequency of $B220^+GL\text{-}7^+CD95^+NP^+$ GC B cells of total $B220^+$ B cells. **(E)** Representative flow plot of total $IgD^-CD138^+TACI^+$ PCs. **(F)** Gating strategy for different subsets of PCs. **(G)** Percentages of subsets of PCs (total $IgD^-CD138^+TACI^+$ PCs, $IgD^-CD138^+TACI^+B220^{int}CD19^+$ plasmablasts, $IgD^-CD138^+TACI^+B220^-CD19^+$ immature PCs, and $IgD^-CD138^+TACI^+B220^-CD19^-$ mature/resting PCs). **(H)** Representative flow and dot plots of $NP^+IgD^-CD138^+TACI^+$ PCs. **(I and J)** Frequencies of (I) $CD4^+CD44^+CD62L^-$ splenic effector and (J) $CD4^+CD44^+CD62L^-CXCR5^+PD\text{-}1^+$ Tfh of total $CD4^+$ T cells. **(K and L)** (K) High-affinity (NP4) and (L) low-affinity (NP28) anti-NP and total serum IgG and IgG1 titers. Each symbol represents an individual mouse (n = 7–10 mice per group), and data are presented as means ± SEM. Data in each panel represent two experiments. P values were calculated via an unpaired Student's t test (A–J) or two-way ANOVA with Dunn–Sidak correction (K and L) (NS, not significant, $P > 0.05$; *, $P < 0.05$; **, $P < 0.01$).

GC B cells and much higher expression in $Fc\gamma RIIB^{-/-}$ B cells than in B6 control B cells (Fig. 9, A and B). We also analyzed the published RNAseq dataset (Jenks et al., 2018) and found higher IRF7 expression in SLE B cells than in healthy control B cells (Fig. 9 C). In addition, we analyzed IRF7 expression in transitional 3, resting naïve, activated naïve, double negative (DN2) B cells, switched memory, and plasmablast/plasma cells (ASCs) from healthy and SLE samples. *IRF7* expression was increased in activated B cells in SLE patients (Fig. 9 D) and during activation of B cells from healthy peripheral blood mononulcear cells (PBMCs) for 24 h with a TLR7 agonist (Fig. 9 E).

Next, to determine whether IRF7 functioned in a B cell–intrinsic manner to promote spontaneous autoimmune GC and PC responses and autoantibody production, we generated

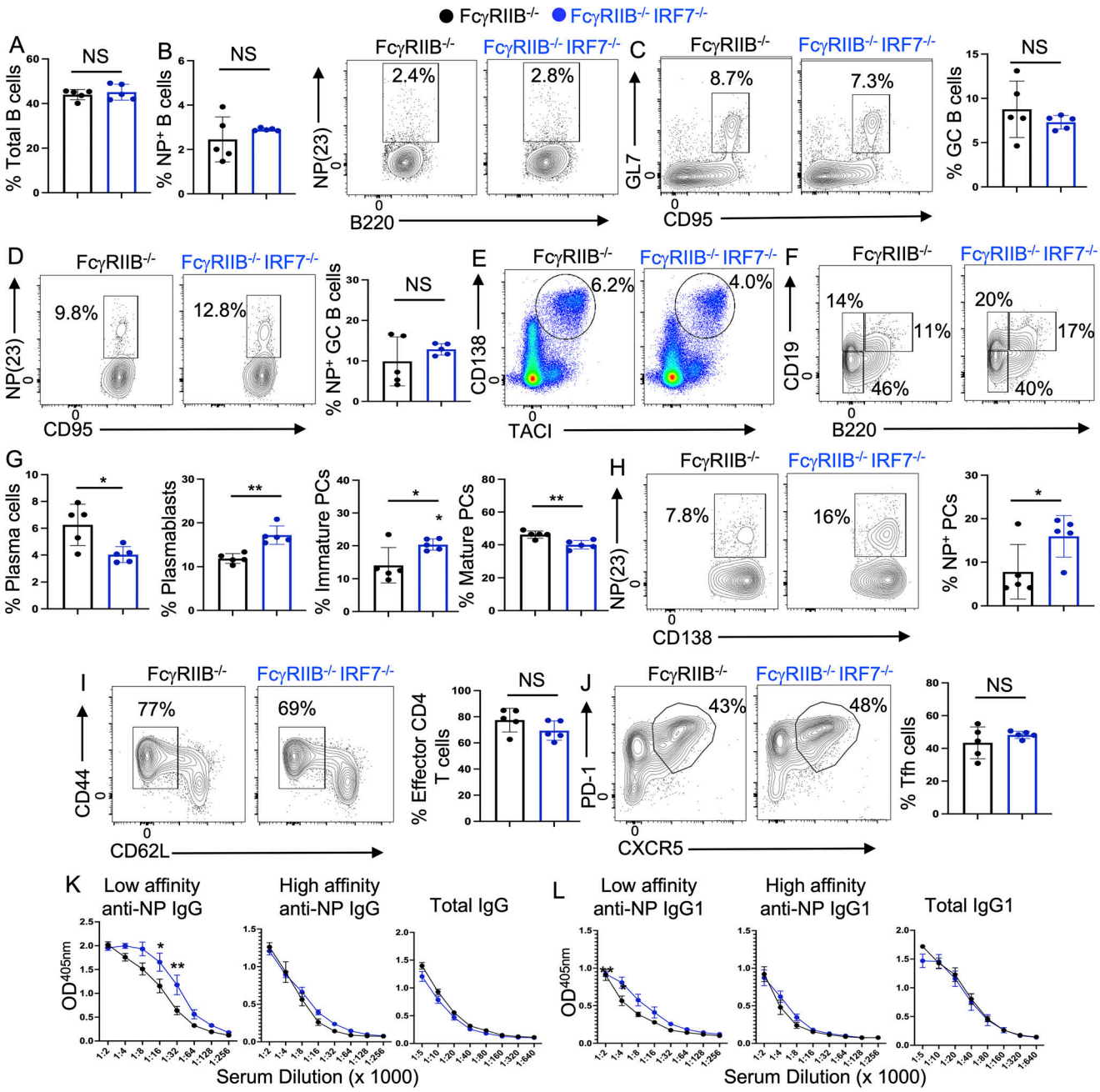

Figure 4. **IRF7 signaling is dispensable for foreign antigen–specific GC, PC, and Ab responses in autoimmune-prone mice.** 16- to 17-wk-old age- and sex-matched FcγRIIB$^{-/-}$ (black circles) and FcγRIIB$^{-/-}$IRF7$^{-/-}$ mice (blue circles) were immunized with NP-KLH in CFA as described in Materials and methods. The splenic GC, PC, and antibody responses were analyzed on 14 days after immunization. **(A and B)** Frequencies of (A) CD19^{+}B220^{+} total and (B) CD19^{+} B220^{+}NP^{+} B cells. **(C)** Frequency of GL-7^{+}CD95^{+} GC B cells of total CD19^{+} B220^{+} B cells. **(D)** Frequency of NP^{+} cells gated on CD19^{+}B220^{+}GL-7^{+}CD95^{+} B cells. **(E)** Representative flow plot of total PCs gated on IgD^{-}CD138^{+}TACI^{+} cells. **(F)** Gating strategy for different subsets of PCs. **(G)** Percentages of subsets of PCs (total IgD^{-}CD138^{+}TACI^{+} PCs, IgD^{-}CD138^{+}TACI^{+}B220^{int}CD19^{+} plasmablasts, IgD^{-}CD138^{+}TACI^{+}B220^{-}CD19^{+} immature PCs, and IgD^{-}CD138^{+}TACI^{+}B220^{-}CD19^{-} mature/resting PCs). **(H)** Representative flow and dot plots of NP^{+} PCs gated on IgD^{-}CD138^{+}TACI^{+} cells. **(I and J)** Frequencies of (I) CD44^{+}CD62L^{-} splenic effector and (J) CD44^{+}CD62L^{-}CXCR5^{+}PD-1^{+} Tfh of total CD4^{+} T cells. **(K and L)** (K) High-affinity (NP4) and (L) low-affinity (NP28) anti-NP and total serum IgG and IgG1 titers. Each symbol represents an individual mouse (n = 5 mice per group), and data are presented as means ± SEM. Data in each panel represent two experiments. P values were calculated via an unpaired Student's t test (A–J) or two-way ANOVA with Dunn–Sidak correction (K and L) (NS, not significant, P > 0.05; *, P < 0.05; **, P < 0.01).

B cell–specific mixed BM chimeras. 20% BM cells from FcγRIIB$^{-/-}$ or FcγRIIB$^{-/-}$IRF7$^{-/-}$ mice were mixed with 80% BM cells from mu mutant (μMT) mice, which lack B cells, in a 20:80 ratio and transferred into lethally irradiated μMT recipient mice as depicted in Fig. 9 F. This approach created chimeric mice in which B cell compartment was 100% deficient in IRF7 and non-B cell compartment (T cells and myeloid cells) was 80% wild type with 20% IRF7 deficient. Serum ANA positivity

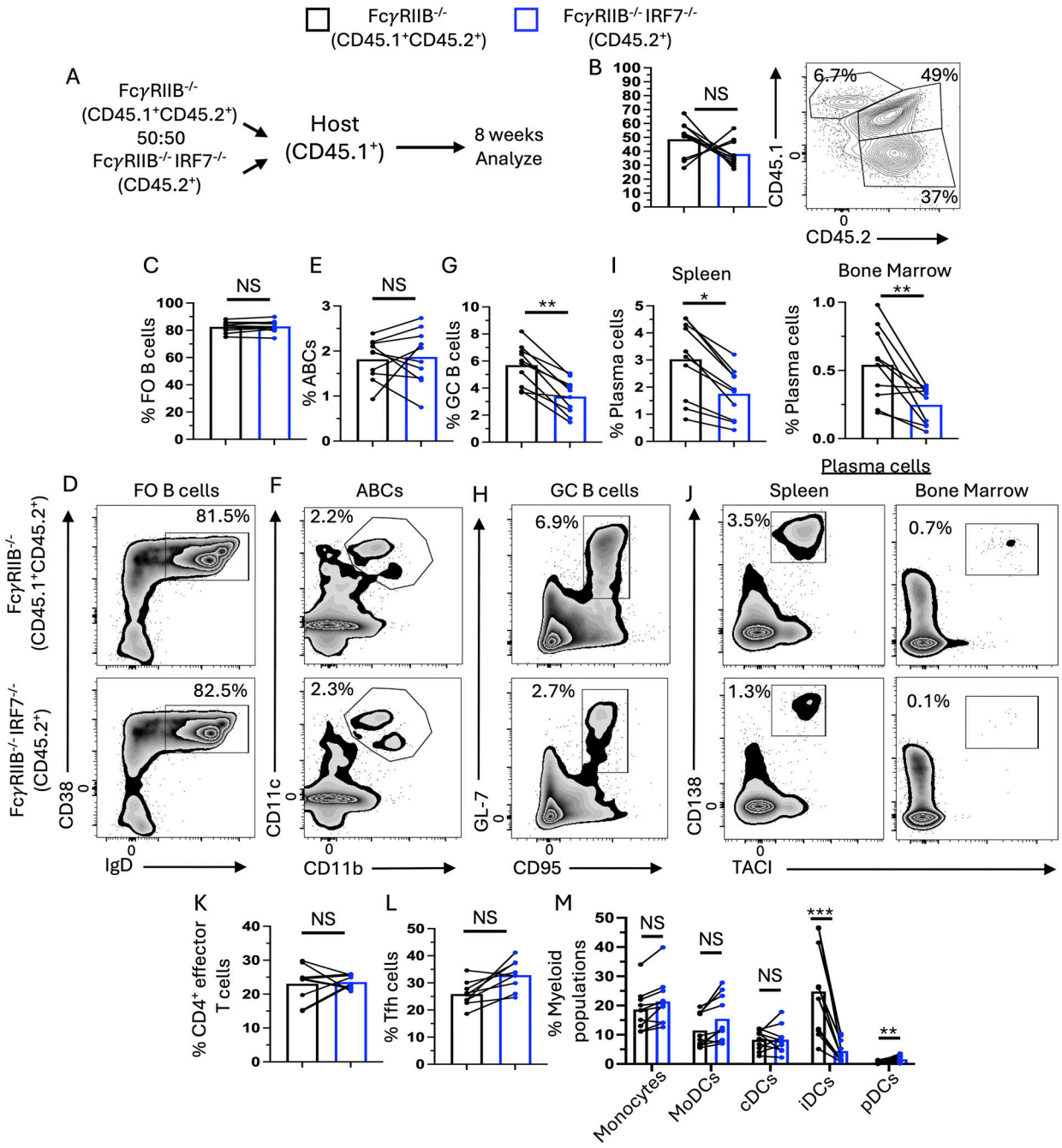

Figure 5. **IRF7 controls autoimmune GC and AFC responses by functioning in hematopoietic cells. (A)** The schematic of competition chimeras in which allotype-marked BM from FcγRIIB$^{-/-}$ (CD45.1$^+$CD45.2$^+$) and FcγRIIB$^{-/-}$IRF7$^{-/-}$ (CD45.2$^+$) mice was transferred into lethally irradiated CD45.1$^+$ hosts. **(B)** The bars and flow cytometry plot show BM reconstitution of FcγRIIB$^{-/-}$ (CD45.1$^+$CD45.2$^+$) and FcγRIIB$^{-/-}$IRF7$^{-/-}$ (CD45.2$^+$) donor cells. **(C and D)** Flow cytometry analysis of (C) the frequency and (D) gating strategy of CD38$^+$IgD$^+$ FO B cells of total B220$^+$CD19$^+$ splenic B cells. **(E–H)** Flow cytometry analysis of (E) the frequency and (F) gating strategy of IgD$^-$CD11b$^+$CD11c$^+$ ABCs of B220$^+$CD19$^+$ total splenic B cells and (G) the frequency and (H) gating strategy of B220$^+$GL-7$^+$CD95$^+$ GC B cells of B220$^+$CD19$^+$ total splenic B cells. **(I and J)** Flow cytometry analysis of (I) the frequency and (J) gating strategy of CD138$^+$TACI$^+$ splenic and BM PCs of IgD$^-$ B cells (shown in Fig. 1 H). **(K–M)** Flow cytometry analysis of the frequencies of splenic (K) CD4$^+$ Teffs and (L) Tfh of total CD4$^+$ cells and (M) the frequencies of various myeloid cells of total myeloid populations. Each symbol represents an individual mouse (n = 10–14 mice per group), and data are presented as means ± SEM. Data in each panel represent three experiments. P values were calculated via an unpaired Student's t test (not significant, NS, P > 0.05; *, P < 0.05; **, P < 0.01; ***, P < 0.001). cDCs, conventional DCs; moDCs, monocyte-derived DCs.

and dsDNA- and SmRNP-reactive autoantibody titers in recipient mice with B cells deficient in IRF7 were significantly reduced compared with recipient mice with B cells sufficient in IRF7 (Fig. 9, G–I). However, no major differences in spleen weight (Fig. 9 J) and frequencies of naïve (Fig. 9 K) and activated (Fig. 9 L) B cell populations were observed between the strains except for an increased percentage of total B cells in the absence of IRF7 in B cells. B cell–specific IRF7-deficient mice

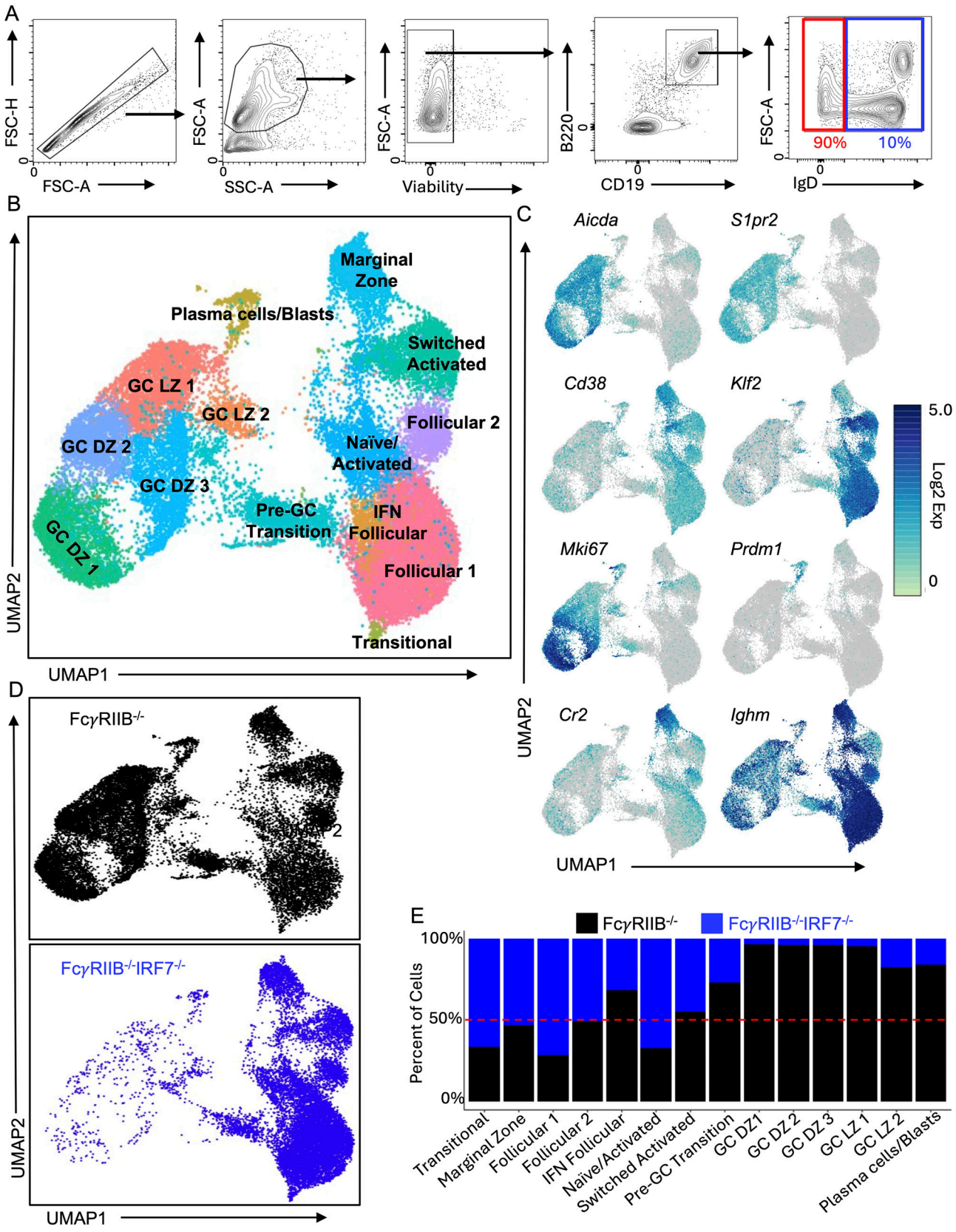

Figure 6. **Single-cell RNAseq identifies 14 clusters in SLE-prone FcγRIIB$^{-/-}$ B cells. (A)** Gating strategy for sorting 90% IgD^{-} activated and 10% IgD^{+} naïve B cells for scRNAseq analysis. Panel A is duplicated in Fig. S5. **(B)** Unsupervised clustering of 36,842 splenic B cells from 3-mo-old FcγRIIB$^{-/-}$ and FcγRIIB$^{-/-}$IRF7$^{-/-}$ mice, visualized using UMAP. Cells analyzed contained 10% B220^{+}IgD^{+} naïve and 90% B220^{+}IgD^{-} activated B cells that were sorted from two individual FcγRIIB$^{-/-}$ and FcγRIIB$^{-/-}$IRF7$^{-/-}$ mice (n = 4 mice). **(C)** Representative UMAPs of hallmark genes to demonstrate annotation of populations in the

scRNAseq dataset. Gene expression for clusters is shown at a log scale. **(D)** UMAPs depicting the distribution of cells between the FcγRIIB$^{-/-}$ and FcγRIIB$^{-/-}$IRF7$^{-/-}$ mice. **(E)** The percentage of cells in each B cell cluster from FcγRIIB$^{-/-}$IRF7$^{-/-}$ and FcγRIIB$^{-/-}$ and mice is shown in the bar graphs. LZ, light zone; DZ, dark zone.

had reduced frequencies of total CD4 and CD4 Teffs, although no differences in the frequency of Tfh (Fig. 9 M) and myeloid cells (Fig. 9 N) were observed between the strains. These data indicate a B cell–intrinsic requirement of IRF7 in loss of immune tolerance, autoantibody production to DNA- and RNA-associated autoantigens, and CD4$^+$ Teff responses, whereas both B cell–intrinsic and –extrinsic contributions of IRF7 are required for driving GC, PC, and Tfh cell responses in SLE-like autoimmunity.

Discussion

Despite a longstanding association of IRF7 with SLE, the cell-intrinsic role and mechanism by which IRF7 promotes spontaneous SLE-associated GC and PC responses that harbor autoreactive B cells in SLE are not known. Here, using IRF7-deficient mice, competitive mixed BM, and B cell–specific BM chimeras, we identified previously unknown B cell–intrinsic and –extrinsic roles for IRF7 in promoting spontaneous autoimmune GC and PC responses. We found that IRF7 is involved in B cell differentiation into autoantibody-producing cells, steady-state total and ANA-specific class-switched IgG antibody responses, and SLE pathogenesis. IRF7, however, was dispensable for promoting foreign antigen–driven GC, PC, and antibody responses. Through the single-cell transcriptome analysis of SLE-prone B cells, we uncovered the functions for IRF7-driven transcriptional programs in B cell differentiation through pre-GC into GC and PC pathways during systemic autoimmune responses. Analysis of ChIP-seq data identified IRF7 target genes that are differentially expressed in IRF7-deficient SLE-prone B cells. Mechanistically, IRF7 promotes systemic autoimmunity by regulating B cell transcriptome, translation, and metabolism required for B cell activation and differentiation into GC and PC populations during SLE-like autoimmune responses.

Previous studies highlighted the roles of both the extrafollicular (EF) (Jenks et al., 2018; William et al., 2002) and GC pathways (Arkatkar et al., 2017; Cappione et al., 2005; Degn et al., 2017; Jackson et al., 2016; Soni et al., 2014; Tiller et al., 2010; Vinuesa et al., 2009) in the development of autoreactive B cells and pathogenic Ab production in SLE-prone mice and patients. In particular, using the FcγRIIB$^{-/-}$ SLE mouse model used in the current study, Tiller et al. previously showed the development of autoreactive GC B cells and PCs in which IgG autoantibodies were enriched in GCs and somatically hypermutated (Tiller et al., 2010), highlighting the role of the GC pathway in pathogenic autoantibody production. By blocking the GC pathway, previous studies highlighted a pathogenic role for the EF pathway in systemic autoimmunity (Brown et al., 2022; Voss et al., 2022). We observed dampened GC and PC responses, low numbers of autoantibody-producing splenic and BM AFCs, and reduced serum ANA titers in FcγRIIB$^{-/-}$ mice in the absence of IRF7. Together, our current findings and the previously described role of the GC pathway in pathogenic Ab production in FcγRIIB$^{-/-}$ mice (Tiller et al., 2010) strongly suggest the role of IRF7 in the generation of autoreactive PCs and pathogenic Abs through the GC pathway. Several studies have demonstrated that ABCs generated through EF pathways can either differentiate into EF plasmablasts or participate within the GC (Nickerson et al., 2023; Ricker et al., 2021). Deeper understanding of the differential mechanisms by which GC and EF pathways promote high-affinity autoantibody-producing PCs in SLE is warranted to develop targeted therapeutics.

Previous studies have delineated the contributions of IRF5, including a B cell–intrinsic role of IRF5, in promoting systemic autoimmunity and disease (Ban et al., 2021; Banga et al., 2020; Cham et al., 2012; Pellerin et al., 2021; Richez et al., 2010). Here, for the first time, we identified the role of IRF7 in promoting PC and GC responses and autoantibody production. It is thought that there is a significant overlap between IRF5 and IRF7 functions; however, it is not clear whether IRF7 homodimerizes or heterodimerizes with IRF5 or other IRF family members (i.e., IRF3) in B cells to promote GC and PC responses in systemic autoimmunity. The family of IRF proteins is well-known to participate in transcriptional coregulation of gene expression (Andrilenas et al., 2018). Studies focusing on the dynamic interactions and the transcriptional landscape regulated by IRF proteins singularly or cooperatively will help develop a deeper understanding of the mechanisms of IRF7-mediated regulation of B cell responses in SLE.

Through the generation of B cell–specific BM chimeras, we show here a B cell–intrinsic requirement of IRF7 in loss of tolerance and autoantibody production. Our data suggest that B cell–intrinsic IRF7 controls GC and/or PC tolerance checkpoints of autoreactive B cell selection. Our BM chimeric data, OMICS, and mechanistic data together suggest that IRF7-regulated transcriptional programs, translation, and metabolic reprogramming in B cells play critical roles in breaking tolerance and autoreactive B cell selection. B cell–intrinsic IRF7 deficiency, however, was not sufficient to affect overall spontaneous PC, GC, and Tfh responses. These data suggest that development of PC, GC, and Tfh responses in the BM chimeric environment requires both B cell–intrinsic and –extrinsic IRF7. Although correlative, IRF7 is thought to contribute to SLE in a B cell–extrinsic manner by inducing T1-IFNs in pDCs (Honda et al., 2005; Huang et al., 2015; Swiecki and Colonna, 2015). Whether B cell–extrinsic IRF7 contributions to autoimmune PC, GC, and Tfh responses in SLE models are mediated by pDC-derived T1-IFN signaling remain to be delineated, especially given that IRF7 deficiency promoted an increased frequency of pDCs in our competitive BM chimeric mice (Fig. 5 M). Interestingly, in the same chimeric mice, we observed a fivefold reduction in the frequency of iDCs in the absence of IRF7 (Fig. 5 M). We also observed reduced number of iDCs in the kidneys of IRF7-deficient FcγRIIB$^{-/-}$Yaa mice. DCs played a

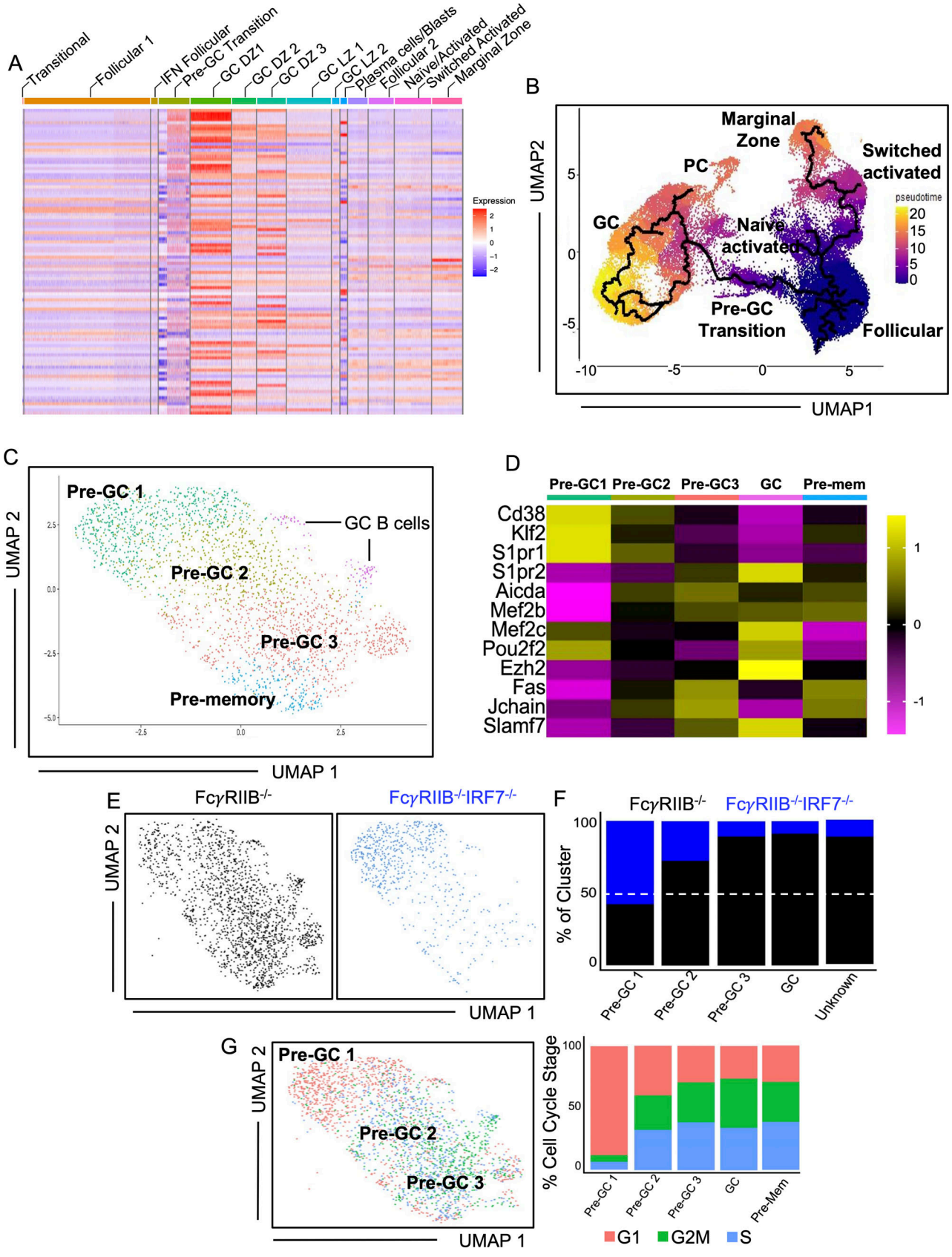

Figure 7. **Single-cell RNAseq delineates the role of IRF7 in B cell differentiation through GC and PC fates. (A)** Top 100 differentially expressed genes across the scRNAseq dataset were analyzed among all clusters. **(B)** Pseudotime analysis of the scRNAseq dataset projected using the UMAP to transcriptionally predict the differentiation projection of follicular B cells in FcγRIIB$^{-/-}$ mice. **(C and D)** (C) Subclustering of the pre-GC transitional cluster (n = 2,461 cells) of

splenic B cells from FcγRIIB$^{-/-}$ mice using (D) markers associated with B cell differentiation into GC B cells. **(E)** Cell cycle analysis of cells in these subclusters. **(F)** The cells in subclusters were compared between FcγRIIB$^{-/-}$ and FcγRIIB$^{-/-}$IRF7$^{-/-}$ mice. **(G)** The percentages of cells in each subcluster from FcγRIIB$^{-/-}$ and FcγRIIB$^{-/-}$IRF7$^{-/-}$ mice that are in the cell cycle are shown in the bar graphs. LZ, light zone; DZ, dark zone.

major role in priming T cells and in SLE development (Klarquist et al., 2016; Seitz and Matsushima, 2010). Given our data from the BM chimera experiments that indicated both B cell–intrinsic and –extrinsic roles of IRF7, delineation of the mechanism by which pDCs and iDCs contribute to autoimmune PC, GC, Tfh, and autoAb responses in SLE models is warranted. Identifying such mechanisms will require an in vivo system, not yet available, in which IRF7 can be deleted in iDCs and pDCs in SLE-prone mice.

Several risk variants in and around IRF7 are associated with SLE disease activity (Fu et al., 2011; Salloum et al., 2010). A mutation in the IRF7 gene resulting in Q412R is associated with elevated IRF7 expression and an increased T1-IFN signature in SLE patients (Fu et al., 2011). However, it has remained unclear whether the IRF7 risk allele contributed to autoimmune GC and PC responses in SLE in a cell–intrinsic manner independent of T1-IFN production. Generation of mouse models carrying IRF7 risk variants will help address this unanswered question. Here, we have demonstrated that outside of the T1-IFN genes, IRF7 can regulate genes in GC B cells and PCs that are involved in translation and metabolism, which are critical for B cell differentiation through GC and PC pathways in a systemic autoimmune response.

A previous study demonstrated the role of IRF7 in promoting autoantibody responses in a chemically (pristane)-induced B6 model of SLE (Miyagawa et al., 2016). Surprisingly, despite reductions in IC deposition in the kidney of IRF7$^{-/-}$ mice, kidney pathology and proteinuria were reported in these mice (Miyagawa et al., 2016). The role of IRF7 in autoimmune GC and PC responses and disease in spontaneous SLE models, which may involve differential mechanisms to drive autoimmunity, has remained unclear. We observed reductions in autoantibody production, IC deposition, kidney pathology, and serum BUN/creatinine levels in IRF7-deficient spontaneous SLE-prone mice. We also observed significantly improved survival in TLR7-accelerated SLE-prone mice deficient in IRF7. Our data suggest that IRF7 plays a major role in promoting GC and PC responses and systemic autoimmunity, including tissue inflammation and disease. The discrepancy between our findings and the previous study could be due to differences in the involvement of differential mechanisms between the spontaneous SLE-prone versus chemically induced non-autoimmune B6 mouse models that were used.

We utilized scRNAseq analysis to profile subpopulations of B cells and their differentiation trajectories in SLE-prone mice. Pseudotime trajectory analysis of differentiating B cells revealed that during a systemic autoimmune response, B cells differentiate into two distinct pathways in which one group differentiated through a pre-GC transitional bridge into GC and PC fates, and the other group into naïve activated and switched activated B cells. By comparing single-cell transcriptomic data of FcγRIIB$^{-/-}$ and FcγRIIB$^{-/-}$IRF7$^{-/-}$ B cells, we discovered a significant deficit in IRF7$^{-/-}$ B cell differentiation into GC and plasmablasts/PC clusters. Through targeted re-clustering of pre-GC transitional cells, we further discovered that B cell differentiation was halted at the pre-GC1 stage in the absence of IRF7, in which the majority of these cells were quiescent compared with B cells in FcγRIIB$^{-/-}$ mice that progressed to pre-GC2 and pre-GC3 stages and were in the cell cycle. Our OMICs and validation data together suggest that during autoimmune B cell responses in spontaneous SLE-prone mice, IRF7 induces transcription of genes required for protein translation and metabolism in B cells. These IRF7-driven events in B cells, together with B cell–extrinsic factors, likely T1-IFN signaling, are required to meet the demands of activated B cells that can differentiate into GC and PC fates, promoting the generation of pathogenic autoantibody-producing cells and leading to SLE development.

Limitations of the study

Our identification of critical B cell–intrinsic and –extrinsic roles for IRF7 in regulating their differentiation into the GC and PC pathways does not negate the potential IRF7 role in regulating other B cell populations. Although we focused on the role of IRF7 in B cell differentiation into the GC/PC clusters, we identified differentially expressed genes in the naïve activated, switched activated, and MZ B cell clusters that will be a topic of further investigation at the mechanistic level. Additionally, based on our current findings suggesting both B cell–intrinsic and –extrinsic roles for IRF7 in autoimmune GC and PC responses and in the loss of B cell tolerance in systemic autoimmunity, we primarily focused our investigations into the IRF7 role in B cell responses. We, however, cannot exclude the possibility that IRF7 may contribute to the functionality of myeloid or T cell populations and thereby contribute to the autoimmune B cell response and autoimmunity. Thus, interrogation of IRF7 functions in other cell types in promoting autoimmune GC and PC responses and systemic autoimmunity also will be necessary in the future.

Materials and methods

Study design

The overall goal of this study was to delineate the cell-intrinsic and -extrinsic mechanisms by which IRF7 promotes autoimmune B cell responses in systemic autoimmunity. This was accomplished by first generating IRF7-deficient, SLE-prone mice and then by generating competitive and B cell–specific mixed BM chimeras. The phenotypic examination of various B and T cell populations was performed by flow cytometry and immunofluorescence (IF) microscopy. Mechanistic studies were performed through single-cell transcriptome and ChIP-seq of B cells from SLE-prone mice sufficient and deficient in IRF7. The number of mice per experiment was determined based on the power calculation of our published data (Chodisetti et al., 2020;

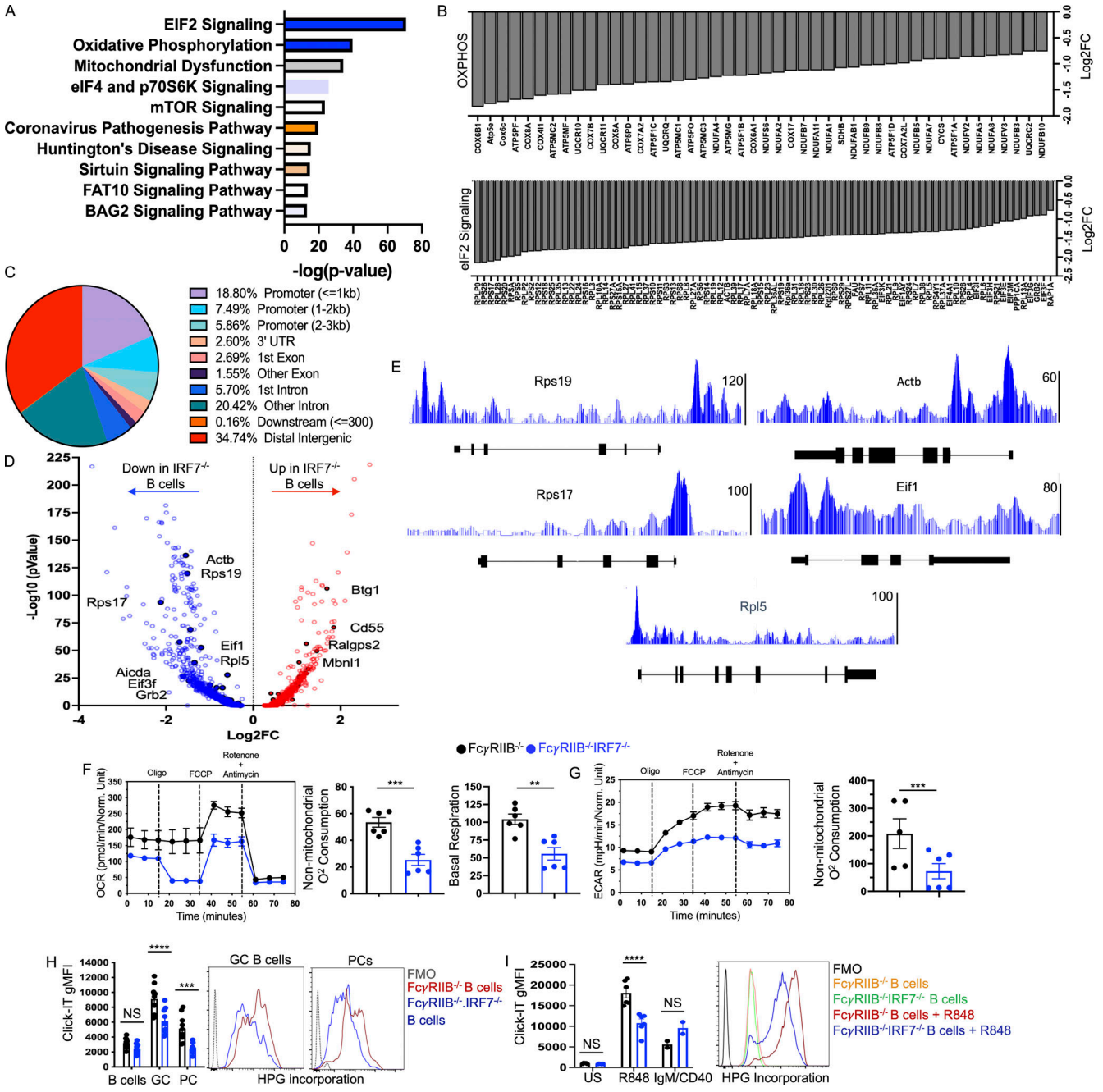

Figure 8. **IRF7 regulates translation and metabolism during B cell activation. (A)** Ingenuity pathway analysis of differentially expressed genes within the pre-GC clusters of the scRNAseq data from FcγRIIB$^{-/-}$ and FcγRIIB$^{-/-}$IRF7$^{-/-}$ mice. **(B)** The heatmaps of upregulated and downregulated genes linked to EIF2 signaling and OXPHOS between FcγRIIB$^{-/-}$ and FcγRIIB$^{-/-}$IRF7$^{-/-}$ pre-GC clusters. **(C)** The pie chart showing the genomic locations of IRF7 peaks from ChIP-seq analysis of antigen-experienced IgD^{-} B cells from FcγRIIB$^{-/-}$ mice. **(D)** The volcano plot of IRF7 target genes identified by ChIP-seq analysis, which are up-regulated and downregulated between FcγRIIB$^{-/-}$ and FcγRIIB$^{-/-}$IRF7$^{-/-}$ B cells in scRNAseq analysis. **(E)** Representative IRF7 peaks in the promoters of several ribosomal protein genes. **(F and G)** Extracellular flux analysis showing OXPHOS and glycolysis of FcγRIIB$^{-/-}$IRF7$^{-/-}$ and FcγRIIB$^{-/-}$ B cells, including basal respiration and non-mitochondrial OCR. **(H)** Translation analysis in total and spontaneously activated B cells from FcγRIIB$^{-/-}$ and FcγRIIB$^{-/-}$IRF7$^{-/-}$ mice. **(I)** Analysis of translation in TLR7-activated B cells from FcγRIIB$^{-/-}$ and FcγRIIB$^{-/-}$IRF7$^{-/-}$ mice by flow cytometry. Data in A–E represent four mice. Each symbol in F–I represents an individual mouse (n = 3–6 mice per group), and data are presented as means ± SEM. Data in F–I represent two to four experiments. P values were calculated via an unpaired Student's t test (F and G) or two-way ANOVA with Dunn–Sidak correction (H and I) (not significant, NS, P < 0.05; **, P < 0.01; ***, P < 0.001; ****, P < 0.0001).

Domeier et al., 2018; Fike et al., 2021). Littermate controls were used where possible. Control and experimental mice were age- and sex-matched. All data points generated in various experiments were included in the analysis. All experimental findings were replicated, and the number of replicates is indicated in the figure legends.

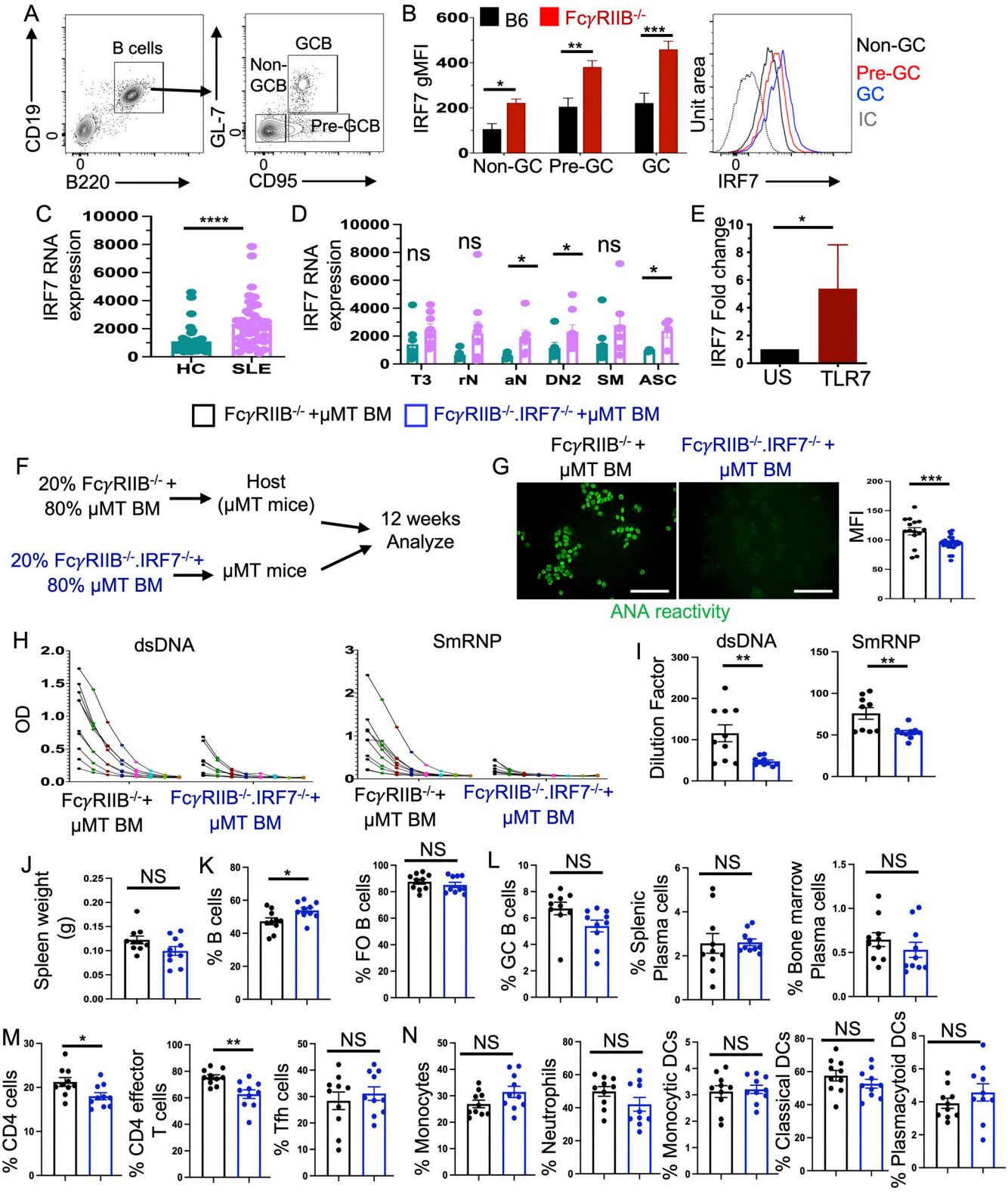

Figure 9. **B cell–intrinsic and –extrinsic roles of IRF7 in breaking tolerance and autoimmune PC and GC responses. (A)** Gating strategy of B220⁺CD19⁺GL-7⁻CD95⁻ non-GC B cells (non-GCB), B220⁺CD19⁺GL-7⁻CD95⁺ pre-GC B cells (pre-GCB), and B220⁺CD19⁺GL-7⁺CD95⁺ GC B cells (GCB). **(B)** IRF7 expression in geometric mean fluorescent intensity (gMFI) in non-GCB, pre-GCB, and GCB cells in B6 and FcγRIIB⁻/⁻ mice. **(C and D)** Our analysis of published RNAseq data of healthy control (HC) and SLE patients showing IRF7 RNA expression in total (C) and various subsets of B cells (D), such as transitional 3 (T3), resting naïve (rN), activated naïve (aN), double negative (DN2) B cells, switched memory (SM), and plasmablast/PCs (ASCs). **(E)** *IRF7* expression was measured in B cells from healthy PBMCs following activation for 24 h with a TLR7 agonist. **(F)** Schematic of B cell–specific mixed BM chimeric mice generation. **(G–I)** (G) Immunofluorescent staining of Hep-2 slides for serum ANA seropositivity (Scale bars, 100 μm) and (H and I) serum anti-dsDNA and anti-SmRNP antibody titers

in μMT recipient mice with FcγRIIB$^{-/-}$ B cells sufficient and deficient IRF7. RNA expression in HC and SLE patient B cells. **(J–L)** Spleen weight and frequencies of B220^{+} total and FO B cells, GC B cells, splenic plasma, and bone PCs of B220^{+} total B cells. **(M)** Flow cytometry analysis of frequencies of CD4^{+} total T cells, CD4^{+} Teffs, and Tfh cells of total CD4^{+} T cells. **(N)** Flow cytometry analysis of frequencies of splenic myeloid cells in these mice. Each symbol represents an individual mouse (n = 9–10 mice per group), and data are presented as means ± SEM. Data in each panel represent two independent experiments. P values were calculated via two-way ANOVA with Dunn–Sidak correction (B) or an unpaired Student's t test (C–E and G–N) (NS, not significant; *, P < 0.05; **, P < 0.01; ***, P < 0.001; ****, P < 0.0001).

Mice

C57BL/6 (B6), B6.SJL-*Ptprc*^{a}*Pepc*^{b}*/BoyJ* (CD45.1), and B6.129S2-Igh^{tm1Cgn}/J (B6.μMT) mice were originally purchased from the Jackson laboratories and bred in-house. B6.129P2-*Irf7*^{tm1Ttg}/TtgRbRc (IRF7$^{-/-}$) mice were purchased from Riken BRC and bred internally. FcγRIIB$^{-/-}$ mice described previously (Bolland et al., 2002; Shinde et al., 2018) were backcrossed to B6 for several generation before we further backcrossed to B6 for at least N12–14 generation. These mice were intercrossed and then crossed with IRF7-deficient (FcγRIIB$^{-/-}$IRF7$^{-/-}$) mice. The genome scan of FcγRIIB$^{-/-}$ and FcγRIIB$^{-/-}$IRF7$^{-/-}$ mice from our colony performed by the Jackson Laboratories showed that FcγRIIB$^{-/-}$ and FcγRIIB$^{-/-}$IRF7$^{-/-}$ mice contained >99% and >97% B6 genome, respectively. FcγRIIB$^{-/-}$yaa mice were generated by crossing FcγRIIB$^{-/-}$ mice to B6.yaa mice (from the Jackson Laboratories) internally. All crosses generated for this manuscript were performed in-house. All animal studies were conducted at Pennsylvania State University Hershey Medical Center in accordance with the guidelines approved by our Institutional Animal Care and Use Committee. Animals were housed in a specific pathogen–free barrier facility.

Generation of mixed BM chimeras

Mixed competition BM chimeric mice

These mice were generated by lethally irradiating 10–12-wk-old female CD45.1 hosts in two doses of 450 rads (X-RAD 320iX Research Irradiator; Precision X-Ray) within a 4-h interval. Within a few hours of irradiation, each recipient mouse received 10 × 10^{6} T cell–depleted BM cells intravenously composed of 5 × 10^{6} cells from FcγRIIB$^{-/-}$ CD45.1^{+}/CD45.2^{+} and 5 × 10^{6} cells from FcγRIIB$^{-/-}$IRF7$^{-/-}$CD45.2^{+} donors (50:50). Recipient mice were analyzed 8 wk after BM reconstitution.

B cell–specific mixed BM chimeras

8–10-wk-old female B6.μMT (B6.129S2-Igh^{mtm1}Cgn/J) recipient mice were lethally irradiated with 900 rads of x rays (X-RAD 320iX Research Irradiator; Precision X-Ray). Within 4–6 h after irradiation, each recipient intravenously received 10^{7} T cell–depleted BM cells isolated from 8 to 10-wk-old female donor mice, with 80% of cells from B6.μMT mice and 20% from FcγRIIB$^{-/-}$ or FcγRIIB$^{-/-}$IRF7$^{-/-}$ mice. Recipients were analyzed after 3 mo.

Immunization of mice

Age- and sex-matched non-autoimmune B6 (8–10 wk old) and autoimmune-prone FcγRIIB$^{-/-}$ (16–17 wk old) mice were immunized i.p. with 200 μg of NP-KLH (Biosearch Technologies) mixed with CFA (Sigma-Aldrich). Spleens were harvested and processed for various analyses on indicated day after immunization.

Flow cytometry

Analysis of splenic populations was performed by processing the tissue into a single-cell suspension followed by RBC lysis using Tris-ammonium chloride. Splenocytes were stained using the antibodies listed in the table below (Table 1). For BM analysis, cells were flushed from isolated femurs with RPMI, followed by RBC lysis and staining. For the flow cytometry of the kidney, the kidneys were perfused prior to harvesting. Kidneys were minced into small pieces using a scalpel and incubated with collagenase Type I (Sigma-Aldrich) for 30 min at 37°C prior to RBC lysis and staining. For intracellular staining, cells were fixed using BD Cytofix (BD Biosciences) and permeabilized using BD Phosflow Perm Buffer III according to the manufacturer's instructions. Staining of unfixed cells was performed at 4°C except for anti-CXCR5 Ab, which was performed at room temperature. Stained cells were analyzed on a BD LSR II or BD FACSymphony A3 (BD Biosciences) using FACSDiva Software. Sorting experiments were performed on a BD ARIA SORP high-performance cell sorter (BD Biosciences). Flow cytometry data were analyzed using FlowJo Software version 10.8.1 (BD) (Table 1).

Kidney histopathology and scoring

Kidneys from 6-mo-old mice were fixed in 10% neutral buffered formalin and embedded in paraffin. Kidney sections were cut at 3-μm thickness for periodic acid–Schiff. The slides were scanned on a TissueGnostics TissueFAXS SL imaging system with Kromnigon Spectra Split 7 filters and the TissueFAXS 71.1.138 software. Renal disease was evaluated with a semiquantitative 0–4+ scale as described (Chan et al., 1997). The scale was used for each compartment (glomerular, interstitial, and vascular), with the pathology graded according to specified criteria as absent (0–1), mild (1–2), moderate (2–3), or severe (3–4+). For comparative purposes, all the tissue sections were scored by one observer (R. Caricchio), who was blinded to the origin of the kidney samples.

ELISA

To detect serum ANAs, ELISA plates (Thermo Fisher Scientific) were first coated with poly-L-lysine, followed by salmon sperm dsDNA (Invitrogen), nucleosome (histone from Sigma-Aldrich on a layer of dsDNA coating), or SmRNP (Arotec Diagnostics). To detect NP-specific Abs, plates were coated with 10 μg/ml NP4-BSA or NP29-BSA. Plates were washed and blocked with 5% FBS in PBS, and serum was added starting at a 1:50 dilution in 5% FBS, followed by 1:2 serial dilution for the remainder of the plate. Antibodies were then detected with one of the following biotinylated antibodies: goat anti-mouse IgM (Jackson Immunoresearch Laboratories), goat anti-mouse IgG (Jackson

Table 1. **Key resources table**

Reagent or resource	Source	Identifier
Antibodies		
CD45R (B220) BV605 (RA3-6B2)	BioLegend	Cat: 103244; RRID: AB_2563312
CD45R (B220) Pacific Blue (RA3-6B2)	BD Biosciences	Cat: 558108; RRID: AB_397031
CD45R (B220) PE-Cy5 (RA3-6B2)	Invitrogen	Cat: 35045282; RRID: AB_469721
CD45R (B220) BUV496 (RA3-6B2)	BD Biosciences	Cat: 612950; RRID: AB_2870227
CD19 BV605 (6D5)	BioLegend	Cat: 115540; RRID: AB_2563067
CD19 BV480 (1D3)	BD Biosciences	Cat: 566167; RRID: AB_2739509
T and B cell Activation Antigen FITC (GL-7)	BD Biosciences	Cat: 553666; RRID: AB_394981
T and B cell Activation Antigen Pacific Blue (GL-7)	BioLegend	Cat: 144614; RRID:AB_2563292
CD95 PE-Cy7 (Jo2)	BD Biosciences	Cat: 557653; RRID: AB_396768
CD138 PE-Cy7 (281-2)	BioLegend	Cat: 142514; RRID: AB_2562198
CD138 APC (281-2)	BioLegend	Cat: 142506; RRID: AB_10962911
CD138 BV786 (281-2)	BD Biosciences	Cat: 740880; RRID: AB_2740530
CD138 BV421 (281-2)	BioLegend	Cat: 142508; RRID: AB_11203544
TACI PE (8F10)	BioLegend	Cat: 133404; RRIR: AB_2240584
TACI Alexa Fluor 647 (8F10)	BD Biosciences	Cat: 558453; RRID: AB_647119
IgD APC (11–26c.2a)	BD Biosciences	Cat: 560868; RRID: AB_10612002
IgD Alexa Fluor 700 (11–26c.2a)	BioLegend	Cat: 405730; RRID: AB_2563341
CD4 Alexa Fluor 700 (RM4–5)	BioLegend	Cat: 100536; RRID: AB_493701
CD4 PE (GK1.5)	BD Biosciences	Cat: 553730; RRID: AB_396634
CXCR5 Biotin (2G8)	BD Biosciences	Cat: 551960; RRID: AB_394301
CD44 APC (IM7)	BioLegend	Cat: 103012; RRID: AB_312963
CD62L PE-Cy7 (MEL-14)	BioLegend	Cat: 104418; RRID: AB_313103
Streptavidin PE-Cy5	BioLegend	Cat: 405205
CD38 BUV395 (90/CD38)	BD Biosciences	Cat: 740245; RRID: AB_2739992
IRF7 Purified (SC0617)	Novus Biologicals	Cat: NBP2–67634
IRF7 PE (MNGPKL)	Thermo Fischer Scientific	Cat: 12–5829-82; RRID: AB_2572629

Table 1. **Key resources table (*Continued*)**

Reagent or resource	Source	Identifier
NK1.1 Biotin (PK136)	BioLegend	Cat: 108704; RRID: AB_313391
CD90.2 Biotin (53-2.1)	BD Biosciences	Cat: 553002; RRID: AB_394540
CD19 Biotin (1D3)	BD Biosciences	Cat: 553784; RRID: AB_395048
CD11c BV421 (N418)	BioLegend	Cat: 117330; RRID: AB_11219593
CD11b Alexa Fluro 700 (M1/70)	BD Biosciences	Cat: 557960; RRID: AB_396960
Ly6C FITC (AL-21)	BD Biosciences	Cat: 553104; RRID: AB_394628
Streptavidin PE	BioLegend	Cat: 405204
CD8a BV605 (53-6.7)	BioLegend	Cat: 100744; RRID: AB_2562609
Ly6G BV711 (1A8)	BioLegend	Cat: 127643; RRID: AB_2565971
MHCII PE-Cy7 (M5/114.15.2)	BioLegend	Cat: 107630; RRID: AB_2069376
Fixable Viability Dye eFluor 780	eBioscience	Cat:65–0865-14
TruStain FcX (93)	BioLegend	Cat: 101320; RRID: AB_1574975
CD45.1 PE (A20)	BD Biosciences	Cat: 561872; RRID: AB_395044
CD45.1 BV650 (A20)	BD Biosciences	Cat: 563754AB_2738405
CD45.2 BUV661 (104)	BD Biosciences	Cat: 741516; RRID: AB_2870965
Ly6G Pacific Blue (1A8)	BioLegend	Cat: 127612; RRID: AB_2251161
CD317 APC (927)	BioLegend	Cat: 127015; RRID: AB_1967101
NK1.1 BUV563 (PK136)	BD Biosciences	Cat: 741233; RRID: AB_2870785
CD45 BUV805 (30-F11)	BD Biosciences	Cat: 748370; RRID: AB_2872789
CD44 PE-CF594 (IM7)	BD Biosciences	Cat: 562464; RRID: AB_11153123
F4/80 BB700 (T45–2342)	BD Biosciences	Cat: 746070; RRID: AB_2743450
CD4 BUV395 (GK1.5)	BD Biosciences	Cat: 565974; RRID: AB_2738426
IgD BUV737 (217-170)	BD Biosciences	Cat: 749300; RRID: AB_2873674
Goat anti-mouse IgM	Jackson Immunoresearch	Cat: 115-005-020; RRID: AB_2338450
Goat anti-mouse IgG	Jackson Immunoresearch	Cat: 115-005-003020; RRID:AB_2338447
Biotin Goat anti-mouse IgG	Jackson Immunoresearch	Cat: 115-065-003

Table 1. **Key resources table (*Continued*)**

Reagent or resource	Source	Identifier
Biotin Goat anti-mouse IgG1	Invitrogen	Cat: A10519; RRID: AB_1500809
Biotin Goat anti-mouse IgG2c	Southern Biotech	Cat: 1078-08; RRID: AB_2794463
Biotin Goat anti-mouse IgG3	Southern Biotech	Cat: 1100-08; RRID: AB_2794575
Biotin Goat anti-mouse IgG2b	Southern Biotech	Cat: 1090-08; RRID: AB_2794523
Anti-mouse Kappa Biotin	Invitrogen	Cat: RMK15; RRID: AB_2556586
Anti-mouse Kappa FITC (H139-52,1)	Southern Biotech	Cat: 1180-02; RRID: AB_2794678
C3 FITC	Immunology Consultant Laboratory	Cat: GC3-90F-Z
IgG PE	Abcam	Cat: ab37359
Chemicals, peptides, and recombinant proteins		
Collagenase Type I	Worthington	Cat: LS004197
Cycloheximide	Thermo Fisher Scientific	Cat: J66901.03
Puromycin	Sigma-Aldrich	Cat: P7255
L-Homopropargylglycine	Thermo Fisher Scientific	Cat: C10186
NP conjugated with PE	Biosearch Technologies	Cat: N-5070-1
NP-KLH	Biosearch Technologies	Cat: N-5060-25
Complete Freund's Adjuvant	Sigma-Aldrich	Cat: F5881-6X10ML
NP-BSA	Biosearch Technologies	Cat: N-5050H-10 and N-5050XL-10
Deposited data		
scRNAseq data	This paper	Submitted: GSE264033
ChIP-seq data	This paper	Submitted: GSE264034
Experimental models: Organisms/strains		
C57BL/6 (B6)	Jackson Laboratories	RRID:IMSR_JAX:000664
B6.SJL-*Ptprc*^{a}*Pepc*^{b}*/BoyJ* (CD45.1)	Jackson Laboratories	RRID:IMSR_JAX:002014
B6.129P2-*Irf7*^{tm1Ttg}/TtgRbRc	Riken Laboratories	BRC No. RBRC01420
B6.SB-Yaa/J	Jackson Laboratories	RRID:IMSR_JAX:000483
B6;129S-*Fcgr2b*^{tm1Ttk}/J	Jackson Laboratories	RRID:IMSR_JAX:002848
B6.129S2-Igh^{mtm1}Cgn/J	Jackson Laboratories	RRID:IMSR_JAX:002288
Reagents for B cell isolation and various assays		
CD90.2 Depletion (positive Selection)	StemCell Technologies	Cat: 18951
CytoFix	BD Biosciences	Cat: 554722
BD Phosflow Perm Buffer III	BD Biosciences	Cat: 558050
BD Perm/Wash	BD Biosciences	Cat: 554732
4% Paraformaldehyde	Thermo Fisher Scientific	Cat: J61899
Poly-L-Lysine	Sigma-Aldrich	Cat: P8920-100mL
Salmon Sperm DNA	Invitrogen	Cat: 15632011
Histone from calf thymus	Sigma-Aldrich	Cat: H9250-100mg
SmRNP	Arotec Diagnostics	Cat: ATR01–10
Streptavidin-alkalin Phosphatase	Vector Laboratories	Cat: SA-5100
P-nitrophenyl phosphate (disodium salt)	Thermo Fisher Scientific	Cat: 34047
Urea Nitrogen (BUN) Colorimetric Detection Kit	Arbor Assays	Cat: K024-H1
Enzymatic Creatinine Test Kit	Diazyme	Cat: DZ072B-KY1
Vector Blue Alkaline Phosphatase Substrate Kit III	Vector Laboratories	Cat: SK-5300
Hep-2 Slides	Antibodies Incorporated	SKU: 15–112
Qiagen RNeasy Kit	Qiagen	Cat: 74104
RNAlater	Invitrogen	Cat: AM702
High-Capacity cDNA Kit	Thermo Fisher Scientific	Cat: 4374966
Murine B cell isolation Kit	StemCell Technologies	Cat: 19854
EasySep Human B Cell Isolation Kit	StemCell Technologies	Cat:19674
Click-iT Plus Alexa Fluor 488	Thermo Fisher Scientific	Cat: C10641
ChIP Plus Sonication Chromatin IP Kit	Cell Signaling Technologies	Cat: 56383
Software and algorithms		
FlowJo 10.8 and 9	Tree Star	https://www.flowjo.com
GraphPad Prism 10	GraphPad Software	https://www.graphpad.com

Immunoresearch Laboratories), or goat anti-mouse IgG2c (Southern Biotech). Plates were then washed and incubated with streptavidin-alkaline phosphatase (Vector Laboratories). *P*-nitrophenyl phosphate (disodium salt) (Thermo Fisher Scientific) substrate for alkaline phosphatase was used for developing the plates, and plates were read at λ405 nm on Synergy H1 (BioTek Instruments). Serum BUN and creatinine levels were measured via the Urea Nitrogen (BUN) Colorimetric Detection Kit (Arbor Assays) and the Enzymatic Creatinine Test Kit (Diazyme), respectively, according to the manufacturer's instructions. All ELISA plates were read on

Synergy H1 (BioTek Instruments) at the wavelengths indicated by the manufacturer's instructions.

ELISpot

For detection and quantification of autoantibody producing AFCs, multiscreen 96-well filtration ELISpot plates (Millipore Sigma) were coated with salmon sperm dsDNA (Invitrogen), nucleosome (histone from Sigma-Aldrich on a layer of dsDNA coating), or SmRNP (Arotec Diagnostics). To detect NP-specific Abs, ELISpot plates were coated with 10 µg/ml NP4-BSA or NP29-BSA. Plates were blocked with 5% FBS in PBS. 2×10^6 splenocytes suspended in RPMI 1640 (Corning) containing 10% FBS (Hyclone GE), penicillin-streptomycin (Corning), and Glutamax (Corning) were added to the top row and serially diluted by twofold to the remainder of the rows. Plates were washed, and autoantibody-producing AFCs were detected by incubating with biotinylated anti-κ antibody (Invitrogen) followed by streptavidin-alkaline phosphatase (Vector Laboratories). Plates were then washed and developed via Vector Blue Alkaline Phosphatase Substrate Kit III (Vector Laboratories). ELISpot plates were analyzed using an Immunospot S6 Universal M2 (CTL).

IF microscopy and Hep-2 assay

For the detection of ANA seropositivity, serum from mice was diluted 1:50 and incubated on a Hep-2 slide (Antibodies Incorporated). ANAs were then detected using an FITC-rat anti-mouse k antibody (H139-52,1; Southern Biotech). ANA slides were visualized using a Leica DM4000 fluorescence software (Leica Microsystems).

Splenic and kidney IF microscopy was performed by embedding the tissue in OCT compound (Thermo Fisher Scientific) and snap freezing over liquid nitrogen. 5-µM sections were cut and mounted on a ColorFrost Plus Microscope Slide (Thermo Fisher Scientific) and fixed in cold acetone for 20 min. For splenic GC staining, tissue sections were stained with the following antibodies: GL-7 FITC and anti–IgD-APC (11–26c2a; BD Biosciences) and anti–CD4-PE (GK1.2; BioLegend). GC measurements were performed on a random selection of GL-7$^+$ staining across the splenic tissue section where total GC area (μM^2) was measured using the Leica Application Suite Advanced Fluorescence quantification tool. Kidney sections were stained with anti–CD3-FITC (Immunology Consultant Laboratory) and anti–IgG-PE (Abcam) for the detection of IC depositions. Stained tissue sections were imaged on a Leica DM4000 Fluorescence microscope (Leica Microsystems).

Seahorse extracellular flux analysis

Splenic B cells were isolated from indicated mice via negative selection (StemCell Technologies). Cells were resuspended in XF DMEM pH 7.4 media supplemented with 1 mM pyruvate, 2 mM glutamine, and 10 mM glucose and plated on poly-L-lysine–coated microchamber wells. OCRs and extracellular acidification rates were measured using a XF HS mini analyzer (Agilent). For the mito stress test, 1.5 µM oligomycin, 2 µM Carbonyl cyanide 4-(trifluoromethoxy) phenylhydrazone (FCCP), and 0.5 µM antimycin/rotenone were utilized. Data were analyzed using the Agilent Seahorse Wave Software.

Translation assay

Single-cell suspension of splenocytes was prepared as described above. Splenocytes were incubated for 30 min in methionine-free RPMI 1640 medium with 10% of dialyzed FBS at 37°C. Cells were cultured for an additional 2 h for L-Homopropargyl glycine (HPG) incorporation (final concentration 100 µM). Cycloheximide- (100 µg/ml) or puromycin- (10 µg/ml) treated samples were used as negative controls. HPG incorporation in GC B cells and PCs was stained with the Click-iT Plus Alexa Fluor 488 Picolyl Azide Toolkit using the Foxp3 fixation-permeabilization method and was detected by flow cytometry.

Human B cell in vitro stimulation and IRF7 expression

PBMCs were isolated from two healthy donor whole blood samples using a Ficoll gradient (BD) under an Institutional Review Board–approved protocol at Penn State College of Medicine. B cells were then isolated from the PBMCs using StemCell EasySep Human B cell Isolation Kit. Isolated B cells were stimulated overnight with 300 ng/ml of R848 in 10% RPMI. RNA was isolated from B cells by the Qiagen RNeasy Kit (Qiagen) according to the manufacturer's instructions. RNA quality and quantity were assessed via NanoDrop prior to cDNA synthesis (Thermo Fisher Scientific). cDNA was generated using the High-Capacity cDNA Kit (Thermo Fisher Scientific) according to the manufacturer's instructions. TaqMan primers for IRF7 (Hs01014809_g1) were used. Expression levels were normalized by a housekeeping gene (β-actin), and fold change was calculated by the 2(ΔΔCt) method.

scRNAseq and pathway analysis

Spleens from two 3-mo-old FcγRIIB$^{-/-}$ and two FcγRIIB$^{-/-}$IRF7$^{-/-}$ mice were processed for cell sorting as described above. CD3$^-$B220$^+$CD19$^+$IgD$^-$ and CD3$^-$B220$^+$CD19$^+$IgD$^+$ cells were sorted from each animal and mixed at a ratio of 9:1 (IgD$^-$: IgD$^+$) prior to library preparation. Library preparation and sequencing were performed by the Center for Applied Genomics Core at the Children's Hospital of Philadelphia. Libraries were prepared using the 10x Genomics Chromium Single Cell 3′ Reagent Kit v2 as per the manufacturer's instructions. Sequencing was performed on an Illumina HiSeq sequencer. Data were then processed through the CellRanger pipeline (10x Genomics). Demultiplexing and alignments were performed against the mm10 transcriptome. Analysis was performed via Seurat package (v. 4.99) within R. Cells expressing <200 or >4,000 unique genes were excluded from further analysis. Cells with >10% mitochondrial gene expression were also excluded. Log normalization and scaling of features were completed before principal component dimensionality reduction, clustering, and visualization via UMAP. Pseudotime analysis was performed using the Monocle3 package in R. A Wilcoxon rank-sum test with a Bonferroni multiple testing correction was used to identify differentially expressed genes between FcγRIIB$^{-/-}$ and FcγRIIB$^{-/-}$IRF7$^{-/-}$ groups. Gene pathway-based analyses from

the "Pre-GC transition" subclusters were performed using Ingenuity Pathway Analysis Software (Qiagen).

ChIP-seq and analysis

Spleens from 10 5–4-mo-old FcγRIIB$^{-/-}$ mice were pooled in duplicate (five mice in each sample) and processed for cell sorting as described above. CD3^{-}B220^{+}CD19^{+}IgD^{-} B cells were sorted and prepared for ChIP as previously described (Fike et al., 2023). Briefly, cells were fixed using 1.5% formaldehyde for 15 min at 37°C followed by glycine to stop the reaction. Samples were processed further using Cell Signaling ChIP Plus Sonication Chromatin IP Kit (Cell Signaling) according to the manufacturer's instructions, sonication was performed on a Biorupter PICO (Diagenode). Library prep and sequencing were performed by the Center for Applied Genomics Core at the Children's Hospital of Philadelphia. Data were processed and analyzed in Bioconductor. Sequences were aligned to reference genome mm9. Peaks were called against input controls using Macs2. Peaks were visualized in IGV.

Quantification and statistical analysis

All data were plotted as the mean of the data ± SEM, unless otherwise indicated. For all datasets, the normality of the data was first assessed based on the number of samples via D'Agostino–Pearson omnibus normality test or the Shapiro–Wilk normality test. Statistical significance between two groups was determined using the Student's *t* test when two groups were compared. For datasets containing more than two groups and multiple time points, a two-way ANOVA with a Dunn–Sidak correction for multiple comparisons was performed. For the survival curve, a log-rank (Mantel–Cox) test was performed. The statistical test used is denoted in each figure legend. Statistical analyses were performed using Prism GraphPad software version 6 or 10 (GraphPad Software). P values are shown as NS, not significant; *, $P < 0.05$; **, $P < 0.01$; ***, $P < 0.001$; ****, $P < 0.0001$ for significance.

Online supplemental material

Fig. S1 describes the reduced spleen size, splenocyte number, and the early stage serum autoantibody titers in the absence of IRF7. Fig. S2 describes the reduced numbers of steady-state IgG1- and IgG2c-producing AFCs and total serum IgG1 and IgG2c titers in the absence of IRF7. Fig. S3 evaluates the effects of IRF7 deficiency on the number of myeloid cells in SLE-prone FcγRIIB$^{-/-}$ mice. Fig. S4 analyzes the numbers of splenic and BM AFCs and myeloid cell populations. Fig. S5 identifies the B cell clusters through the analysis of single-cell transcriptome of SLE-prone B cells from IRF7-sufficient and -deficient FcγRIIB$^{-/-}$ mice.

Data availability

All data are available in the main text or in the supplementary materials. scRNAseq (accession number GSE264033) and ChIP-seq (accession number GSE264034) data have been deposited at the NCBI Gene Expression Omnibus and are publicly available. Accession numbers are also listed in Table 1. Any additional information required to reanalyze the data reported in this paper will be available from the lead contact upon request.

Acknowledgments

We would like to thank the Pennsylvania State University Hershey Medical Center flow cytometry core facility and Department of Comparative Medicine for help with flow cytometric experiments and animal housing and care, respectively. We thank the support staff within the central facility of the Department of Microbiology and Immunology at Pennsylvania State University College of Medicine. We would like to acknowledge the contributions of Dr. Renata Pellegrino Da Silva, Fernanda Thompson, Jacqueline Smiler, and the other members of the Center for Applied Genomics at CHOP for their help with the scRNAseq and ChIP-seq. We acknowledge the Sanderson Center for Optical Experimentation (SCOPE), Massachusetts Life Science Cener (the SCOPE RRID is SCR_022721) and Leah Whiteman for technical assistance.

This work was primarily supported by the National Institutes of Health grant to Z.S.M. Rahman: RO1 AI162971. This project was partially funded by the following grants: The Judy S. Finkelstein Memorial Research Award at the PennState College of Medicine (A.J. Fike), American Association of Immunology Careers in Immunology Fellowship (A.J. Fike), National Cancer Institute 5T32CA060395-25 (A.J. Fike), Lupus Foundation of America Goldie Simon Preceptorship Award (A.J. Fike), National Heart Lung and Blood Institute grant to M. Trebak: R35 HL150778, and the Pennsylvania Department of Health Tobacco CURE Funds.

Author contributions: A.J. Fike: conceptualization, data curation, formal analysis, funding acquisition, investigation, methodology, validation, visualization, and writing—original draft, review, and editing. K.N. Bricker: conceptualization, data curation, formal analysis, investigation, methodology, validation, and writing—review and editing. M.V. Gonzalez: data curation, formal analysis, investigation, methodology, software, visualization, and writing—review and editing. A. Maharjan: investigation, validation, and writing—review and editing. T. Bui: resources. K. Nuon: resources. S.M. Emrich: investigation and methodology. J.L. Weber: investigation. S.A. Luckenbill: investigation. N.M. Choi: investigation. R. Sauteraud: formal analysis, software, and visualization. D.J. Liu: data curation, formal analysis, and supervision. N.J. Olsen: resources and writing—original draft, review, and editing. R. Caricchio: formal analysis, investigation, resources, and validation. M. Trebak: conceptualization, funding acquisition, project administration, resources, supervision, validation, and writing—review and editing. S.B. Chodisetti: conceptualization, formal analysis, investigation, methodology, validation, and writing—review and editing. Z.S.M. Rahman: conceptualization, funding acquisition, project administration, supervision, validation, visualization, and writing—review and editing.

Disclosures: The authors declare no competing interests exist.

Submitted: 13 October 2023
Revised: 4 November 2023
Accepted: 1 May 2025

References

Andrilenas, K.K., V. Ramlall, J. Kurland, B. Leung, A.G. Harbaugh, and T. Siggers. 2018. DNA-Binding landscape of IRF3, IRF5 and IRF7 dimers: Implications for dimer-specific gene regulation. *Nucleic Acids Res.* 46: 2509–2520. https://doi.org/10.1093/nar/gky002

Arkatkar, T., S.W. Du, H.M. Jacobs, E.M. Dam, B. Hou, J.H. Buckner, D.J. Rawlings, and S.W. Jackson. 2017. B cell-derived IL-6 initiates spontaneous germinal center formation during systemic autoimmunity. *J. Exp. Med.* 214:3207–3217. https://doi.org/10.1084/jem.20170580

Bagavant, H., and S.M. Fu. 2009. Pathogenesis of kidney disease in systemic lupus erythematosus. *Curr. Opin. Rheumatol.* 21:489–494. https://doi.org/10.1097/BOR.0b013e32832efff1

Ban, T., M. Kikuchi, G.R. Sato, A. Manabe, N. Tagata, K. Harita, A. Nishiyama, K. Nishimura, R. Yoshimi, Y. Kirino, et al. 2021. Genetic and chemical inhibition of IRF5 suppresses pre-existing mouse lupus-like disease. *Nat. Commun.* 12:4379. https://doi.org/10.1038/s41467-021-24609-4

Banga, J., D. Srinivasan, C.C. Sun, C.D. Thompson, F. Milletti, K.S. Huang, S. Hamilton, S. Song, A.F. Hoffman, Y.G. Qin, et al. 2020. Inhibition of IRF5 cellular activity with cell-penetrating peptides that target homodimerization. *Sci. Adv.* 6:eaay1057. https://doi.org/10.1126/sciadv.aay1057

Bolland, S., Y.S. Yim, K. Tus, E.K. Wakeland, and J.V. Ravetch. 2002. Genetic modifiers of systemic lupus erythematosus in FcgammaRIIB(−/−) mice. *J. Exp. Med.* 195:1167–1174. https://doi.org/10.1084/jem.20020165

Brown, G.J., P.F. Cañete, H. Wang, A. Medhavy, J. Bones, J.A. Roco, Y. He, Y. Qin, J. Cappello, J.I. Ellyard, et al. 2022. TLR7 gain-of-function genetic variation causes human lupus. *Nature.* 605:349–356. https://doi.org/10.1038/s41586-022-04642-z

Cappione, A. III, J.H. Anolik, A. Pugh-Bernard, J. Barnard, P. Dutcher, G. Silverman, and I. Sanz. 2005. Germinal center exclusion of autoreactive B cells is defective in human systemic lupus erythematosus. *J. Clin. Invest.* 115:3205–3216. https://doi.org/10.1172/JCI24179

Celhar, T., and A.M. Fairhurst. 2014. Toll-like receptors in systemic lupus erythematosus: Potential for personalized treatment. *Front. Pharmacol.* 5:265. https://doi.org/10.3389/fphar.2014.00265

Cham, C.M., K. Ko, and T.B. Niewold. 2012. Interferon regulatory factor 5 in the pathogenesis of systemic lupus erythematosus. *Clin. Dev. Immunol.* 2012:780436. https://doi.org/10.1155/2012/780436

Chan, O., M.P. Madaio, and M.J. Shlomchik. 1997. The roles of B cells in MRL/lpr murine lupus. *Ann. N. Y. Acad. Sci.* 815:75–87. https://doi.org/10.1111/j.1749-6632.1997.tb52046.x

Chodisetti, S.B., A.J. Fike, P.P. Domeier, S.L. Schell, T.E. Mockus, N.M. Choi, C. Corradetti, B. Hou, H.M. Atkins, R. Caricchio, et al. 2020. Serine phosphorylation of the STAT1 transactivation domain promotes autoreactive B cell and systemic autoimmunity development. *J. Immunol.* 204:2641–2650. https://doi.org/10.4049/jimmunol.2000170

Christensen, S.R., and M.J. Shlomchik. 2007. Regulation of lupus-related autoantibody production and clinical disease by Toll-like receptors. *Semin. Immunol.* 19:11–23. https://doi.org/10.1016/j.smim.2006.12.005

Christensen, S.R., J. Shupe, K. Nickerson, M. Kashgarian, R.A. Flavell, and M.J. Shlomchik. 2006. Toll-like receptor 7 and TLR9 dictate autoantibody specificity and have opposing inflammatory and regulatory roles in a murine model of lupus. *Immunity.* 25:417–428. https://doi.org/10.1016/j.immuni.2006.07.013

Cosgrove, H.A., S. Gingras, M. Kim, S. Bastacky, J.S. Tilstra, and M.J. Shlomchik. 2023. B cell-intrinsic TLR7 expression drives severe lupus in TLR9-deficient mice. *JCI Insight.* 8:e172219. https://doi.org/10.1172/jci.insight.172219

Deane, J.A., P. Pisitkun, R.S. Barrett, L. Feigenbaum, T. Town, J.M. Ward, R.A. Flavell, and S. Bolland. 2007. Control of toll-like receptor 7 expression is essential to restrict autoimmunity and dendritic cell proliferation. *Immunity.* 27:801–810. https://doi.org/10.1016/j.immuni.2007.09.009

Degn, S.E., C.E. van der Poel, D.J. Firl, B. Ayoglu, F.A. Al Qureshah, G. Bajic, L. Mesin, C.A. Reynaud, J.C. Weill, P.J. Utz, et al. 2017. Clonal evolution of autoreactive germinal centers. *Cell.* 170:913–926.e19. https://doi.org/10.1016/j.cell.2017.07.026

Domeier, P.P., S.B. Chodisetti, S.L. Schell, Y.I. Kawasawa, M.J. Fasnacht, C. Soni, and Z.S.M. Rahman. 2018. B-Cell-Intrinsic type 1 interferon signaling is crucial for loss of tolerance and the development of autoreactive B cells. *Cell Rep.* 24:406–418. https://doi.org/10.1016/j.celrep.2018.06.046

Fike, A.J., S.B. Chodisetti, K.N. Bricker, N.M. Choi, Z.C. Chroneos, M.H. Kaplan, and Z.S.M. Rahman. 2021. stat4 is largely dispensable for systemic lupus erythematosus-like autoimmune- and foreign antigen-driven antibody-forming cell, germinal center, and follicular Th cell responses. *Immunohorizons.* 5:2–15. https://doi.org/10.4049/immunohorizons.2000111

Fike, A.J., S.B. Chodisetti, N.E. Wright, K.N. Bricker, P.P. Domeier, M. Maienschein-Cline, A.M. Rosenfeld, S.A. Luckenbill, J.L. Weber, N.M. Choi, et al. 2023. STAT3 signaling in B cells controls germinal center zone organization and recycling. *Cell Rep.* 42:112512. https://doi.org/10.1016/j.celrep.2023.112512

Fu, Q., J. Zhao, X. Qian, J.L. Wong, K.M. Kaufman, C.Y. Yu, M.Y. Mok, J.B. Harley, J.M. Guthridge, Y.W. Song, et al. 2011. Association of a functional IRF7 variant with systemic lupus erythematosus. *Arthritis Rheum.* 63:749–754. https://doi.org/10.1002/art.30193

Green, N.M., A. Laws, K. Kiefer, L. Busconi, Y.M. Kim, M.M. Brinkmann, E.H. Trail, K. Yasuda, S.R. Christensen, M.J. Shlomchik, et al. 2009. Murine B cell response to TLR7 ligands depends on an IFN-beta feedback loop. *J. Immunol.* 183:1569–1576. https://doi.org/10.4049/jimmunol.0803899

Honda, K., H. Yanai, H. Negishi, M. Asagiri, M. Sato, T. Mizutani, N. Shimada, Y. Ohba, A. Takaoka, N. Yoshida, and T. Taniguchi. 2005. IRF-7 is the master regulator of type-I interferon-dependent immune responses. *Nature.* 434:772–777. https://doi.org/10.1038/nature03464

Huang, X., S. Dorta-Estremera, Y. Yao, N. Shen, and W. Cao. 2015. Predominant role of plasmacytoid dendritic cells in stimulating systemic autoimmunity. *Front. Immunol.* 6:526. https://doi.org/10.3389/fimmu.2015.00526

Hwang, S.H., H. Lee, M. Yamamoto, L.A. Jones, J. Dayalan, R. Hopkins, X.J. Zhou, F. Yarovinsky, J.E. Connolly, M.A. Curotto de Lafaille, et al. 2012. B cell TLR7 expression drives anti-RNA autoantibody production and exacerbates disease in systemic lupus erythematosus-prone mice. *J. Immunol.* 189:5786–5796. https://doi.org/10.4049/jimmunol.1202195

Jackson, S.W., H.M. Jacobs, T. Arkatkar, E.M. Dam, N.E. Scharping, N.S. Kolhatkar, B. Hou, J.H. Buckner, and D.J. Rawlings. 2016. B cell IFN-γ receptor signaling promotes autoimmune germinal centers via cell-intrinsic induction of BCL-6. *J. Exp. Med.* 213:733–750. https://doi.org/10.1084/jem.20151724

Jackson, S.W., N.E. Scharping, N.S. Kolhatkar, S. Khim, M.A. Schwartz, Q.Z. Li, K.L. Hudkins, C.E. Alpers, D. Liggitt, and D.J. Rawlings. 2014. Opposing impact of B cell-intrinsic TLR7 and TLR9 signals on autoantibody repertoire and systemic inflammation. *J. Immunol.* 192: 4525–4532. https://doi.org/10.4049/jimmunol.1400098

Jenks, S.A., K.S. Cashman, E. Zumaquero, U.M. Marigorta, A.V. Patel, X. Wang, D. Tomar, M.C. Woodruff, Z. Simon, R. Bugrovsky, et al. 2018. Distinct effector B cells induced by unregulated toll-like receptor 7 contribute to pathogenic responses in systemic lupus erythematosus. *Immunity.* 49:725–739.e6. https://doi.org/10.1016/j.immuni.2018.08.015

Karrar, S., and D.S. Cunninghame Graham. 2018. Abnormal B cell development in systemic lupus erythematosus: What the genetics tell us. *Arthritis Rheumatol.* 70:496–507. https://doi.org/10.1002/art.40396

Klarquist, J., Z. Zhou, N. Shen, and E.M. Janssen. 2016. Dendritic cells in systemic lupus erythematosus: from pathogenic players to therapeutic tools. *Mediators Inflamm.* 2016:5045248. https://doi.org/10.1155/2016/5045248

Laidlaw, B.J., L. Duan, Y. Xu, S.E. Vazquez, and J.G. Cyster. 2020. The transcription factor Hhex cooperates with the corepressor Tle3 to promote memory B cell development. *Nat. Immunol.* 21:1082–1093. https://doi.org/10.1038/s41590-020-0713-6

Miyagawa, F., Y. Tagaya, K. Ozato, and H. Asada. 2016. Essential requirement for IFN regulatory factor 7 in autoantibody production but not development of nephritis in murine lupus. *J. Immunol.* 197:2167–2176. https://doi.org/10.4049/jimmunol.1502445

Nashi, E., Y. Wang, and B. Diamond. 2010. The role of B cells in lupus pathogenesis. *Int. J. Biochem. Cell Biol.* 42:543–550. https://doi.org/10.1016/j.biocel.2009.10.011

Nickerson, K.M., S. Smita, K.B. Hoehn, A.D. Marinov, K.B. Thomas, J.T. Kos, Y. Yang, S.I. Bastacky, C.T. Watson, S.H. Kleinstein, and M.J. Shlomchik. 2023. Age-associated B cells are heterogeneous and dynamic drivers of autoimmunity in mice. *J. Exp. Med.* 220:e20221346. https://doi.org/10.1084/jem.20221346

Ning, S., J.S. Pagano, and G.N. Barber. 2011. IRF7: Activation, regulation, modification and function. *Genes Immun.* 12:399–414. https://doi.org/10.1038/gene.2011.21

Pellerin, A., K. Yasuda, A. Cohen-Bucay, V. Sandra, P. Shukla, B.K.H. Jr, K. Nündel, G.A. Viglianti, Y. Xie, U. Klein, et al. 2021. Monoallelic IRF5 deficiency in B cells prevents murine lupus. *JCI Insight.* 6:e141395. https://doi.org/10.1172/jci.insight.141395

Rawlings, D.J., G. Metzler, M. Wray-Dutra, and S.W. Jackson. 2017. Altered B cell signalling in autoimmunity. *Nat. Rev. Immunol.* 17:421–436. https://doi.org/10.1038/nri.2017.24

Richez, C., K. Yasuda, R.G. Bonegio, A.A. Watkins, T. Aprahamian, P. Busto, R.J. Richards, C.L. Liu, R. Cheung, P.J. Utz, et al. 2010. IFN regulatory factor 5 is required for disease development in the FcgammaRIIB-/-Yaa and FcgammaRIIB-/- mouse models of systemic lupus erythematosus. *J. Immunol.* 184:796–806. https://doi.org/10.4049/jimmunol.0901748

Ricker, E., M. Manni, D. Flores-Castro, D. Jenkins, S. Gupta, J. Rivera-Correa, W. Meng, A.M. Rosenfeld, T. Pannellini, M. Bachu, et al. 2021. Altered function and differentiation of age-associated B cells contribute to the female bias in lupus mice. *Nat. Commun.* 12:4813. https://doi.org/10.1038/s41467-021-25102-8

Salloum, R., B.S. Franek, S.N. Kariuki, L. Rhee, R.A. Mikolaitis, M. Jolly, T.O. Utset, and T.B. Niewold. 2010. Genetic variation at the IRF7/PHRF1 locus is associated with autoantibody profile and serum interferon-alpha activity in lupus patients. *Arthritis Rheum.* 62:553–561. https://doi.org/10.1002/art.27182

Seitz, H.M., and G.K. Matsushima. 2010. Dendritic cells in systemic lupus erythematosus. *Int. Rev. Immunol.* 29:184–209. https://doi.org/10.3109/08830181003602507

Shinde, R., K. Hezaveh, M.J. Halaby, A. Kloetgen, A. Chakravarthy, T. da Silva Medina, R. Deol, K.P. Manion, Y. Baglaenko, M. Eldh, et al. 2018. Apoptotic cell-induced AhR activity is required for immunological tolerance and suppression of systemic lupus erythematosus in mice and humans. *Nat. Immunol.* 19:571–582. https://doi.org/10.1038/s41590-018-0107-1

Soni, C., P.P. Domeier, E.B. Wong, T.N. Shwetank, T.N. Khan, M.J. Elias, S.L. Schell, A.E. Lukacher, T.K. Cooper, and Z.S. Rahman. 2015. Distinct and synergistic roles of FcγRIIB deficiency and 129 strain-derived SLAM family proteins in the development of spontaneous germinal centers and autoimmunity. *J. Autoimmun.* 63:31–46. https://doi.org/10.1016/j.jaut.2015.06.011

Soni, C., E.B. Wong, P.P. Domeier, T.N. Khan, T. Satoh, S. Akira, and Z.S. Rahman. 2014. B cell-intrinsic TLR7 signaling is essential for the development of spontaneous germinal centers. *J. Immunol.* 193:4400–4414. https://doi.org/10.4049/jimmunol.1401720

Swiecki, M., and M. Colonna. 2015. The multifaceted biology of plasmacytoid dendritic cells. *Nat. Rev. Immunol.* 15:471–485. https://doi.org/10.1038/nri3865

Tiller, T., J. Kofer, C. Kreschel, C.E. Busse, S. Riebel, S. Wickert, F. Oden, M.M. Mertes, M. Ehlers, and H. Wardemann. 2010. Development of self-reactive germinal center B cells and plasma cells in autoimmune Fc gammaRIIB-deficient mice. *J. Exp. Med.* 207:2767–2778. https://doi.org/10.1084/jem.20100171

Vinuesa, C.G., I. Sanz, and M.C. Cook. 2009. Dysregulation of germinal centres in autoimmune disease. *Nat. Rev. Immunol.* 9:845–857. https://doi.org/10.1038/nri2637

Voss, L.F., A.J. Howarth, T.R. Wittenborn, S. Hummelgaard, K. Juul-Madsen, K.S. Kastberg, M.K. Pedersen, L. Jensen, A.D. Papanastasiou, T. Vorup-Jensen, et al. 2022. The extrafollicular response is sufficient to drive initiation of autoimmunity and early disease hallmarks of lupus. *Front. Immunol.* 13:1021370. https://doi.org/10.3389/fimmu.2022.1021370

William, J., C. Euler, S. Christensen, and M.J. Shlomchik. 2002. Evolution of autoantibody responses via somatic hypermutation outside of germinal centers. *Science*. 297:2066–2070. https://doi.org/10.1126/science.1073924

Yasuda, K., C. Richez, J.W. Maciaszek, N. Agrawal, S. Akira, A. Marshak-Rothstein, and I.R. Rifkin. 2007. Murine dendritic cell type I IFN production induced by human IgG-RNA immune complexes is IFN regulatory factor (IRF)5 and IRF7 dependent and is required for IL-6 production. *J. Immunol.* 178:6876–6885. https://doi.org/10.4049/jimmunol.178.11.6876

Supplemental material

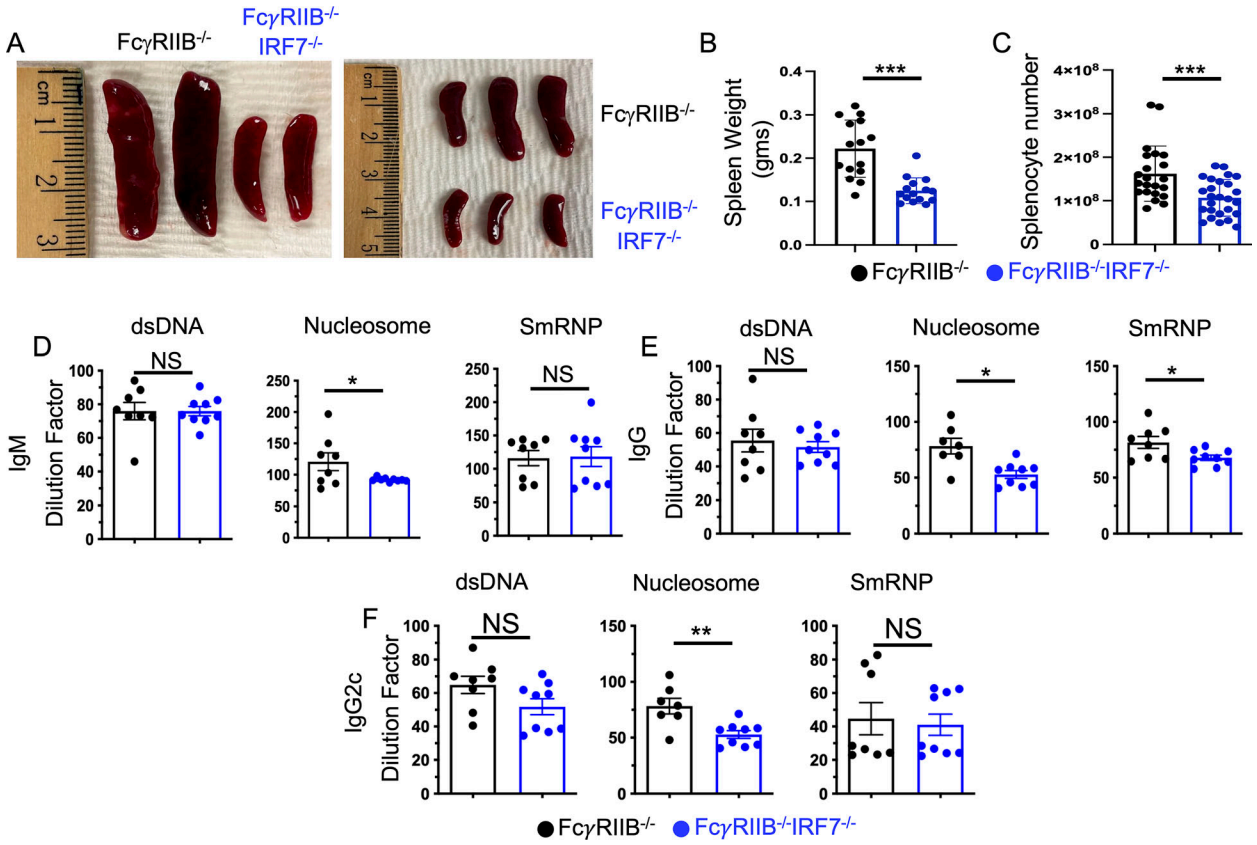

Figure S1. **Reduced spleen size, splenocyte number, and the early stage serum autoantibody titers in the absence of IRF7. (A–F)** Spleen size (A), weight (B), and splenocyte number (C) in 4-mo-old FcγRIIB$^{-/-}$ and FcγRIIB$^{-/-}$IRF7$^{-/-}$ (n = 5 mice per group) mice. dsDNA-, nucleosome-, and Sm/RNP-specific serum IgM (D), IgG (E), and IgG2c (F) titers were measured in 2-mo-old FcγRIIB$^{-/-}$ (n = 8) and FcγRIIB$^{-/-}$IRF7$^{-/-}$ (n = 9) mice by ELISA. Each symbol represents an individual mouse, and data are presented as means ± SEM. P values were calculated via an unpaired Student's t test or Mann–Whitney test (NS, not significant; *, P < 0.05; **, P < 0.01; ***, P < 0.001).

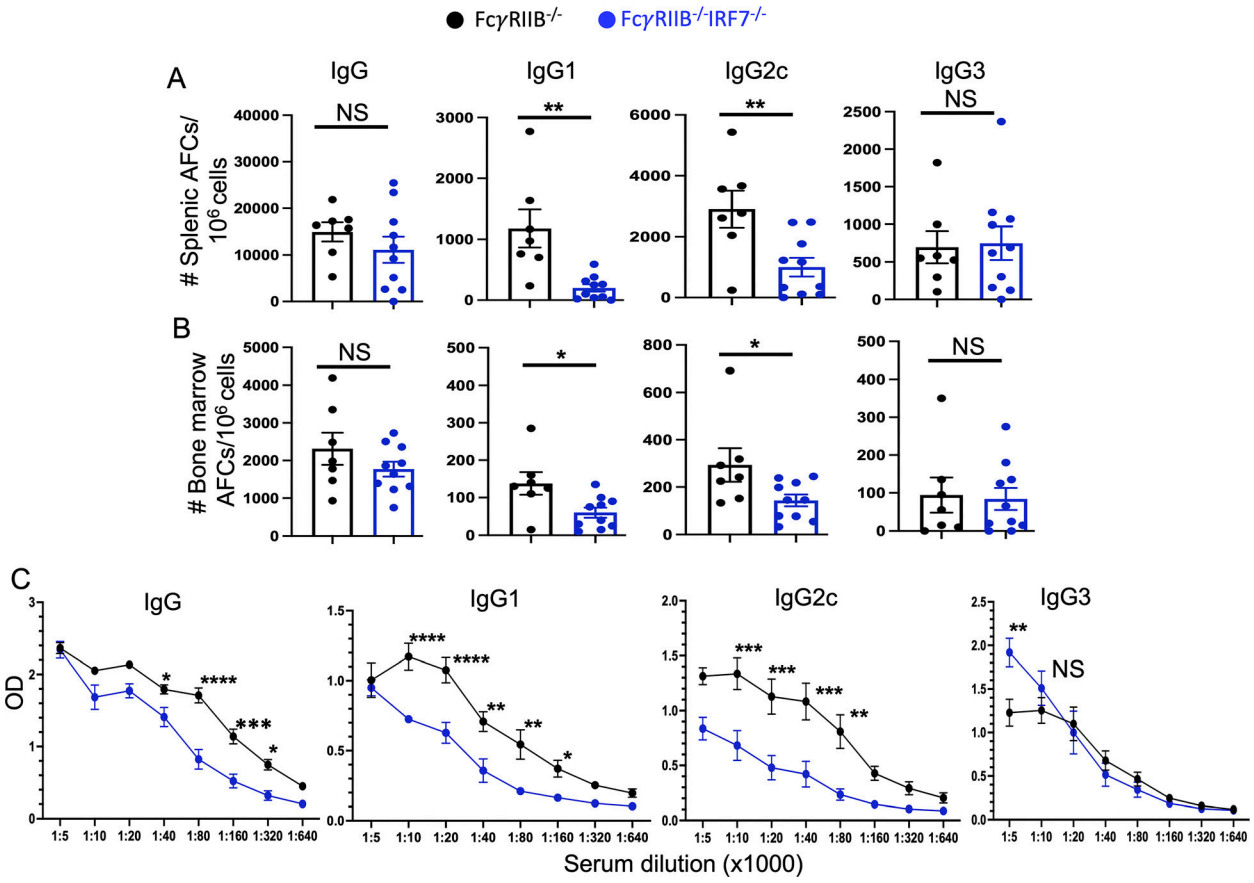

Figure S2. **Reduced numbers of steady-state IgG1- and IgG2c-producing AFCs and total serum IgG1 and IgG2c titers in the absence of IRF7. (A and B)** (A) Numbers of splenic and (B) BM AFCs were enumerated by ELISpot assay. **(C)** Total serum titers of IgG and IgG subclasses (IgG1, IgG2c, and IgG3) in 4-mo-old FcγRIIB$^{-/-}$ and FcγRIIB$^{-/-}$IRF7$^{-/-}$ mice. Each symbol represents an individual mouse, and data are presented as means ± SEM. P values were calculated via an unpaired Student's *t* test or Mann–Whitney test (ns, not significant; *, P < 0.05; **, P < 0.01; ***, P < 0.001; ****, P < 0.0001).

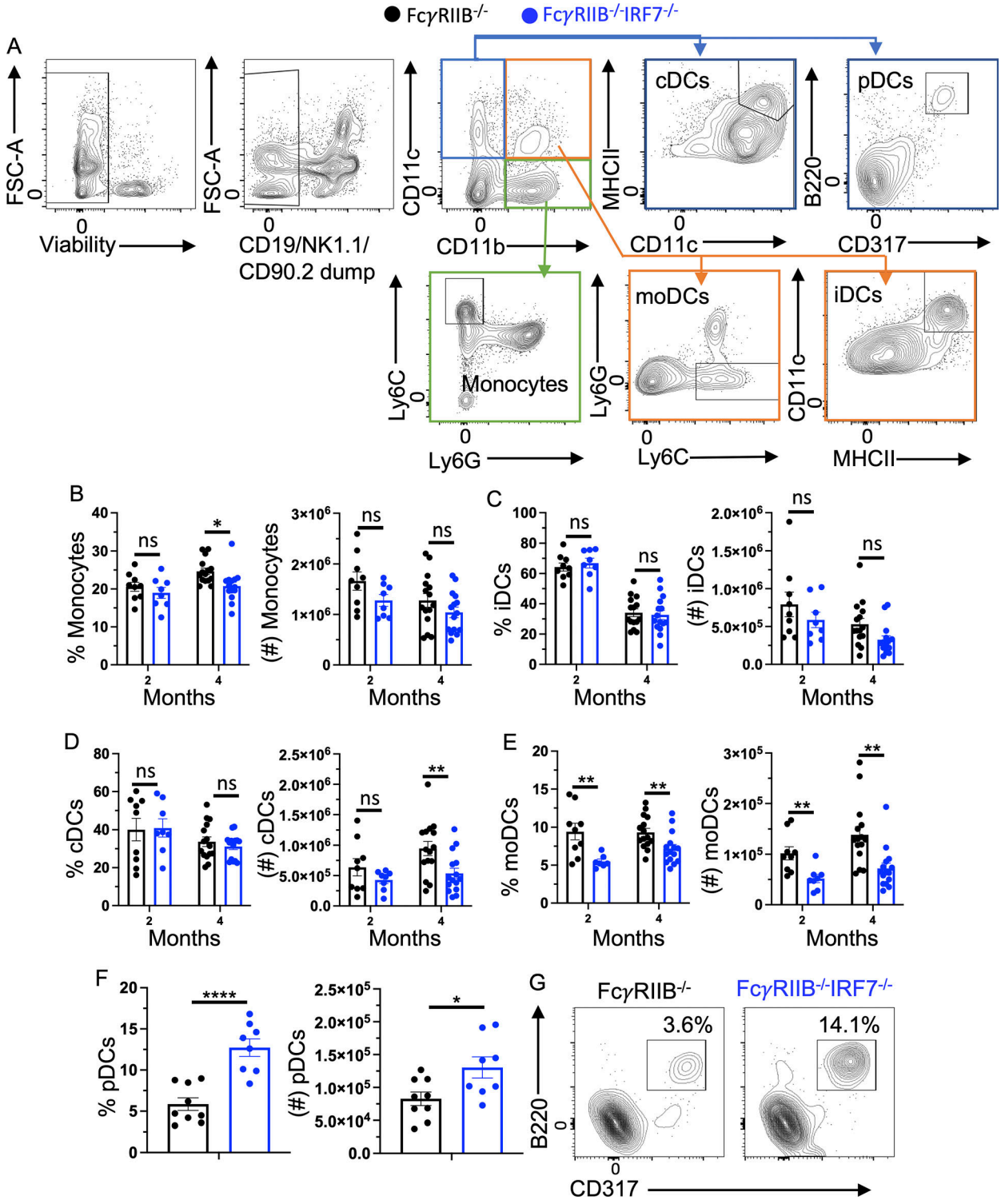

Figure S3. **Reduced number of cDCs and moDCs but increased number of pDCs in IRF7-deficient mice. (A)** The gating strategy of the flow cytometry data showing various myeloid cell populations such as conventional DCs (cDCs), pDCs, monocyte-derived DCs (moDCs), and iDCs. **(B–F)** Percentages and numbers of monocytes (B), iDCs, (C) cDCs, (D) moDCs (E), and pDCs (F) in 2- and 4-mo-old FcγRIIB$^{-/-}$ and FcγRIIB$^{-/-}$IRF7$^{-/-}$ mice (n = 8–9) are shown. **(G)** Gating strategy of B220^{+}CD317^{+} (PDCA-1) pDCs are shown. Each symbol in B–F represents an individual mouse, and data are presented as means ± SEM. Data represent two to three experiments for each time point. P values were calculated via an unpaired Student's t test or Mann–Whitney test (ns, not significant; *, P < 0.05; **, P < 0.01; ****, P < 0.0001).

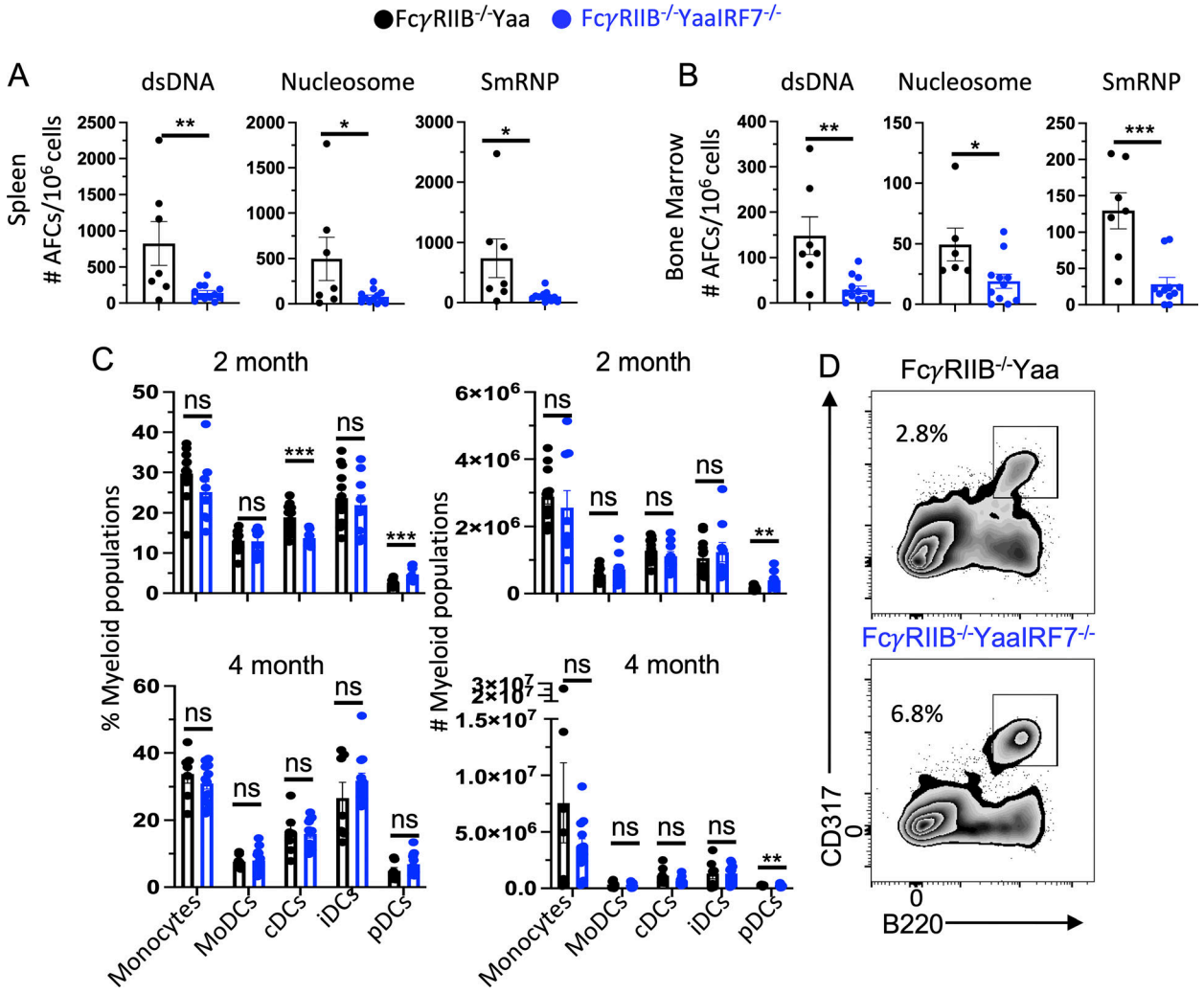

Figure S4. **Reduced autoreactive AFC and increased pDC numbers in FcγRIIB$^{-/-}$YaaIRF7$^{-/-}$ mice. (A and B)** The number of dsDNA-, nucleosome-, and SmRNP-specific splenic (A) and BM (B) AFCs was quantified by ELISpot in 3-mo-old FcγRIIB$^{-/-}$ Yaa and FcγRIIB$^{-/-}$ YaaIRF7$^{-/-}$ mice. **(C)** Percentage and number of myeloid cells in these mice. **(D)** Gating strategy of B220^{+}CD317^{+} (PDCA-1) pDCs. Each symbol represents an individual mouse, and data are presented as means ± SEM. P values were calculated via an unpaired Student's *t* test or Mann–Whitney test (ns, not significant; *, P < 0.05; **, P < 0.01; ***, P < 0.001).

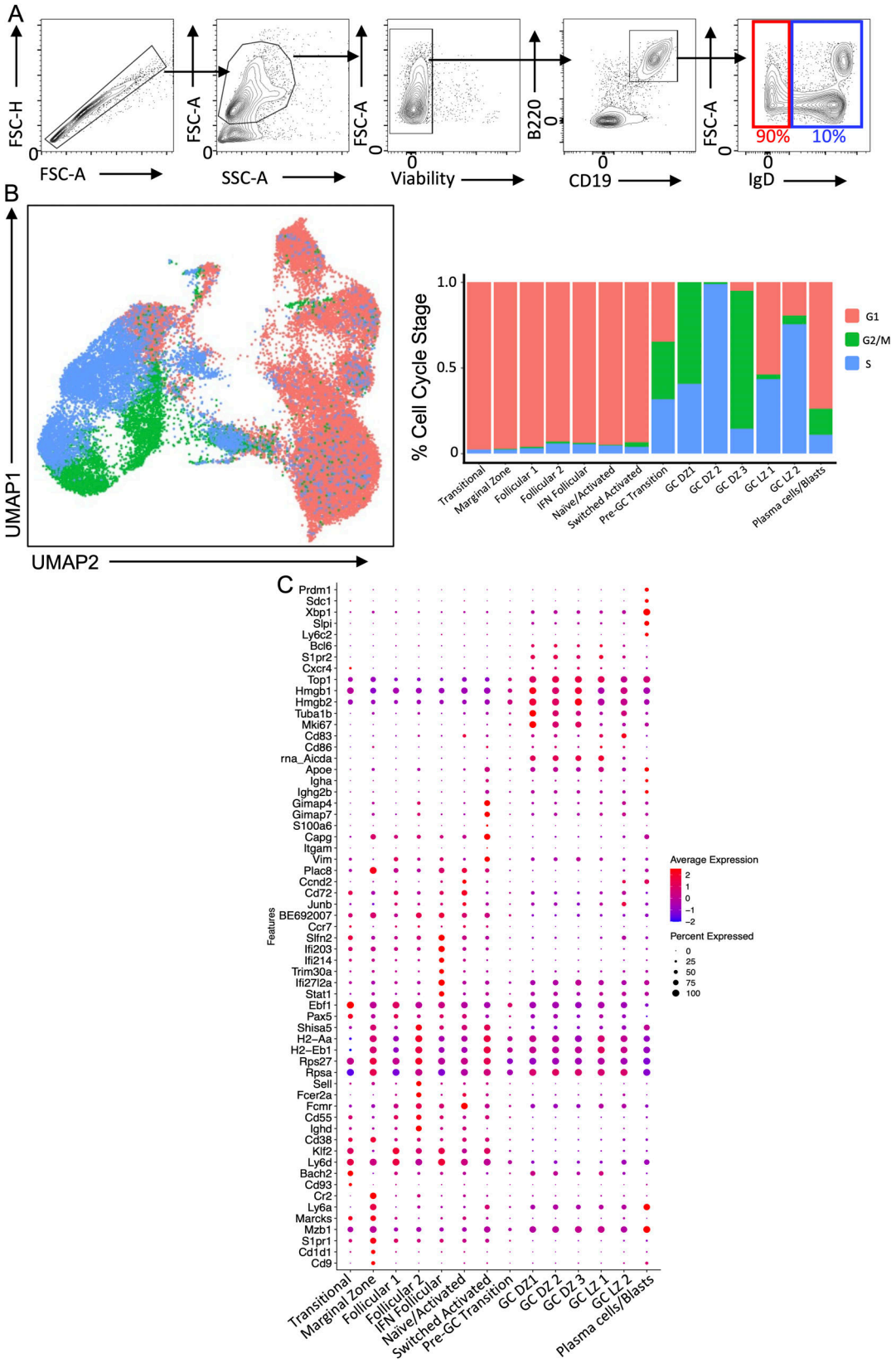

Figure S5. **Single-cell transcriptome of SLE-prone B cells identifies several clusters. (A)** Gating strategy for sorting 90% IgD$^-$ activated and 10% IgD$^+$ naïve B cells for scRNAseq analysis. Panel A is duplicated in Fig. 6. **(B)** UMAP depicting cell cycle status of clusters determined based on average gene expression of gene sets annotated for each cell cycle state. **(C)** Dot plot depicting some major markers used in the annotation of the scRNAseq of B cell clusters, where dot color indicates the average expression of the gene within that cluster and the size of the dot indicates the percentage of the cluster expressing that gene. LZ, light zone; DZ, dark zone.